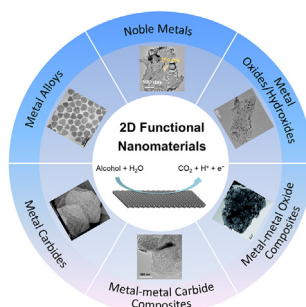Review

Two-dimensional electrocatalysts for alcohol oxidation: A critical review

Xun Zhao[a], Qiming Liu[b], Qiaoxia Li[c], Lingyun Chen[a,b,*], Lei Mao[a], Huayu Wang[a], Shaowei Chen[b,*]

[a] School of Chemistry and Chemical Engineering, Chongqing University, Chongqing 400044, China
[b] Department of Chemistry and Biochemistry, University of California, 1156 High Street, Santa Cruz, CA 95060, United States
[c] College of Environmental and Chemical Engineering, Shanghai University of Electric Power, Shanghai 200090, China

HIGHLIGHTS

- DAFC represents an effective electrochemical energy technology in diverse applications.
- Design and engineering of anode catalysts plays a critical role in the development of DAFC.
- 2D electrocatalysts exhibit unique materials properties and electrocatalytic performances.
- 2D anode catalysts include metals/alloys, metal oxides/hydroxides/carbides, and their nanocomposites.

GRAPHICAL ABSTRACT

ARTICLE INFO

ABSTRACT

Direct alcohol fuel cell (DAFC) exhibits multiple unique advantages, such as high energy conversion efficiency, low cost, ready availability of fuels, minimal environmental pollution, and ease of operation, and has found diverse applications as a small, micro mobile power supply. A critical challenge for the development of DAFC is the design and engineering of effective anode catalysts, where electrooxidation of alcohols occurs. Within this context, two-dimensional (2D) electrocatalysts represent a viable option, due to their unique materials properties, such as large surface area, ease of charge migration and mass transfer, and mechanical robustness during electrochemical reactions. In this review, we summarize recent breakthroughs in the structural engineering of a range of 2D functional nanomaterials, including noble metals and alloys, metal oxides/hydroxides, metal carbides, and precious metal-based nanocomposites, in the electrocatalytic oxidation of alcohols (primarily methanol and ethanol), within the context of reaction mechanisms, and include a perspective highlighting the promises and challenges in future research.

1. Introduction

Development of environmentally friendly energy technologies is an effective strategy to mitigate the energy and environmental issues caused by the consumption of fossil fuels, our primary source of energy so far [1-3]. Of these, fuel cells represent a viable option where chemical energy is efficiently converted into electrical energy with minimal impacts on the environment [4-6]. Among the many types of fuel cells [7-10], direct alcohol fuel cell (DAFC) has been hailed as a promising clean energy technology, where alcohols (e.g., methanol and ethanol) are used as the chemical fuels. Alcohols are in general low-cost, contain a high energy density, and are available from a wide range of (sustainable) sources and safe and convenient in storage and transportation [11-17]. Yet, critical challenges remain. For instance, for
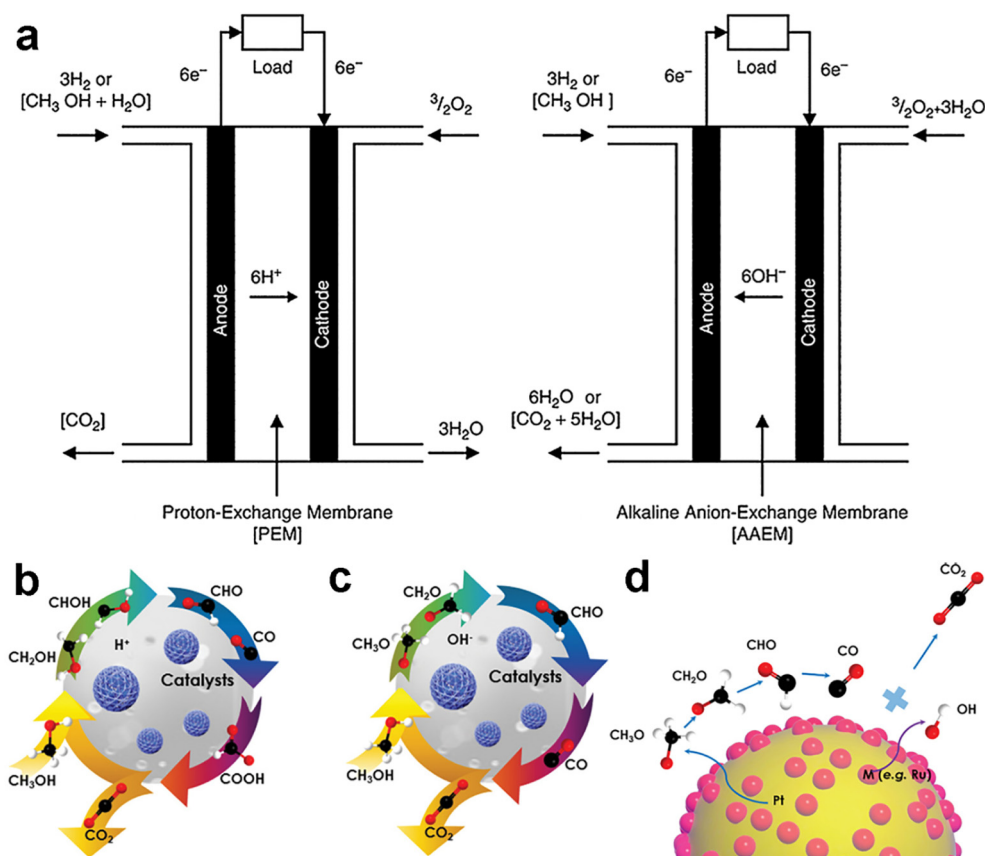
Fig. 1. (a) Schematic presentation of a proton-exchange membrane (PEMFC) and an alkaline membrane fuel cell (AMFC), fueled either with H_2 gas or directly with methanol (DMFC mode). Mechanisms of MOR on the catalysts in (b) acidic and (c) alkaline media. (d) Schematic illustration of the bifunctional mechanism of Pt-based catalysts. (a) Reproduced by permission from Ref. [56]. Copyright (2015) Materials Research Society. (b-d) Reproduced with permission from Ref. [21]. Copyright (2019) Wiley-VCH.

direct methanol fuel cell (DMFC), there remain two major issues that limit the performance, the slow electron-transfer kinetics of anodic methanol oxidation and methanol crossover. The former dictates the rate of proton production and hence the efficiency of power generation, whereas the latter is related to the catharsis ability of the electrolyte. For DAFCs based on more complex alcohols, the overall performance is generally limited due to the lack of efficient catalysts for the cleavage of the $C - C$ bonds and complete oxidation of the alcohols to CO_2 [18-20]. Thus far, platinum-based nanoparticles remain the leading catalysts for alcohol electrooxidation [21-23]. However, the low stability, easy CO poisoning and high cost of Pt have severely hampered the practical applications of DAFC [20,24,25].

Therefore, in recent decades, a wide range of strategies have been employed to improve the electrocatalytic performance of platinum towards alcohol oxidation reaction (AOR) and reduce the operational cost of DAFC [26-28], for instance, by alloying with other (non)noble metals, formation of nanocomposites with carbon derivatives, transition metal oxides/hydroxides, and transition metal carbides [19,29-33], and manipulation of the nanostructure morphologies [34-36]. Alternatively, development of platinum-free AOR catalysts represents another effective strategy. Among these, one-dimensional (1D) electrocatalysts with a highly anisotropic structure are found to facilitate electron transfer, high exposure of active lattice planes, and strong durability during long-term electrocatalytic operation, in comparison with the bulk and nanoparticle counterparts [34,37-39]. Three-dimensional (3D) assemblies of low-dimensional nanostructures are another class of AOR electrocatalysts, which usually exhibit the combined properties of the structural components, an open and porous structure, a large surface area, good chemical and mechanical strength, resistance to aggregation, and high flexibility [40-42]. In fact, 3D AOR electrocatalysts usually have the merits of a high utilization ratio of the active catalysts, abundant active sites, accelerated mass/electron transfer kinetics, and high AOR activity and durability [43,44].

More recently, AOR electrocatalysts based on two-dimensional (2D) nanostructures have also been attracting a great deal of attention. A range of 2D nanostructures have indeed been examined rather extensively in recent studies, such as noble metals and alloys, transition metal dichalcogenides (TMDs), transition-metal carbides and nitrides (MXenes), layered double hydroxides (LDHs), etc., because of their large surface area, shortened charge migration distance, and abundant diffusion channels for ions and molecules [14-17,45]. Notably, the 2D nanostructures can also effectively relieve the stress caused by the volume change and impact damage of bubbles generated by reactions on the material structure, leading to satisfactory electrocatalytic activity and stability. A series of efficient strategies have been reported for the structural engineering of 2D noble metal-based electrocatalysts, such as the precise control of their morphology, thickness, size, porosity, defect, doping, crystal phase, and preferential growth of highly active lattice planes. Such efforts can be aided by theoretical/computational breakthroughs for high-throughput material screening.

Thus, in this review, we will summarize recent research progress of 2D functional nanomaterials as effective electrocatalysts for AOR based on noble metals and alloys, metal oxides/hydroxides, metal carbides, and metal-based composites, within the context of reaction mechanism, performance evaluation and correlation of electrocatalytic activity with material structure. We conclude the review with a perspective highlighting the promises and challenges in future research of 2D functional nanomaterials for AOR electrocatalysis.

2. Noble metals and alloys

Up to now, noble metals and alloys remain the catalysts of choice towards AOR [18]. Electrocatalysts based on 2D nanostructures of noble metals are of particular interest [46], and alloying with another metal is a commonly employed strategy to improve the performance and concurrently to reduce the cost [47]. For instance, Ru is often

selected as the second metal to alloy Pt, due to the strong activity in water dissociation at low potentials, and the electronic effect that facilitates the removal of poisoning intermediates [48].

The complete oxidation of methanol to CO_2 entails the release of 6 electrons and the transfer of 6 OH^-. As the procedures and mechanisms of methanol oxidation reaction (MOR) are widely known (Fig. 1), only the simplified multi-step reactions on a Pt surface in acid media are listed below [49-52],

$$Pt + CH_3OH \rightarrow Pt-CO_{ads} + 4H^+ + 4e^- \qquad (1)$$
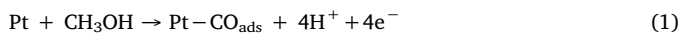
where methanol is firstly adsorbed on the Pt surface, and dehydrogenation leads to the formation of Pt_3-COH as the main intermediate; meanwhile oxidation of the produced $Pt-H$ species to protons is a facile step. Note that the platinum surface is prone to CO poisoning in the absence of active oxygen species (reaction 1). To minimize this poisoning effect, alcohol is best oxidized when a large amount of oxygen-containing species is adsorbed on the electrode surface. This can be facilitated by the incorporation of a second metal (M = Cu, Ni, Ru, Sn, etc) [48,53-55],
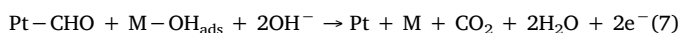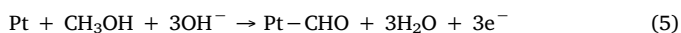
$$M + H_2O \rightarrow M-OH_{ads} + H^+ + e^- \qquad (2)$$
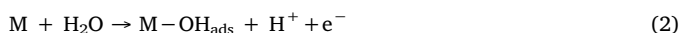
where the generation of surface OH species boosts the further oxidation of CO to CO_2, as manifested in the following reaction,

$$Pt-CO_{ads} + M-OH_{ads} \rightarrow CO_2 + Pt + M + H^+ + e^- \qquad (3)$$
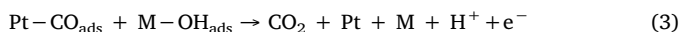
with the total reaction of methanol oxidation on the anode as

$$CH_3OH + H_2O \rightarrow CO_2 + 6H^+ + 6e^- \qquad (4)$$
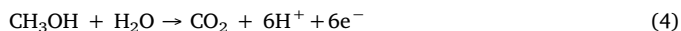
In alkaline media, methanol oxidation on Pt surfaces involves a different reaction pathway [52,57,58],

$$Pt + CH_3OH + 3OH^- \rightarrow Pt-CHO + 3H_2O + 3e^- \qquad (5)$$

$$M + OH^- \rightarrow M-OH_{ads} + e^- \qquad (6)$$

$$Pt-CHO + M-OH_{ads} + 2OH^- \rightarrow Pt + M + CO_2 + 2H_2O + 2e^- (7)$$

Specifically, dehydrogenation of methanol leads to the formation of a series of carbon-containing reaction intermediates, which are then oxidized by oxygen-containing species to produce formate and carbon dioxide. It is generally believed that the oxidation of the CHO_{ads} intermediate to CO_2 is the rate-limiting step (reaction 7). Thus, the rate of methanol oxidation can be enhanced by an increase of the solution pH as well as the incorporation of a second metal into the Pt catalysts, whereby further oxidation of CHO_{ads} is facilitated.

The electrooxidation of more complicated alcohols, such as ethanol [10,11,24,59,60], ethylene glycol [52,61,62], and glycerol [63], involves similar reaction pathways, as it is energetically challenging to break the $C-C$ bond. Understanding these reaction pathways provides a fundamental guideline for the efficient use of the fuels, where the selectivity is critical to obtain desired compounds.

2.1. Noble metals

2D nanostructures of noble metals have emerged as high-performance electrocatalysts for the efficient oxidation of alcohols [46]. For instance, Slabon et al. synthesized 2D arrays of monodisperse Pd nanocrystals by the reduction of $Pd(acac)_2$ with oleylamine (OAm) and borane tributylamine (BTB) at 90 °C for 1 h as efficient electrocatalysts towards both MOR and ethanol oxidation reaction (EOR) [64]. In transmission electron microscopy (TEM) measurements (Fig. 2a), the spherical nanoparticles can be seen to exhibit an average diameter of 7.1 ± 1.1 nm. Electrochemical measurements in the alkaline solution containing 0.5 M NaOH and 1.0 M methanol or ethanol show that the peak current density reached 1040 A g^{-1} (6.7 mA cm^{-2}) for MOR and 5500 A g^{-1} (35.7 mA cm^{-2}) for EOR. This remarkable activity was ascribed to the formation of a 2D array that suppressed agglomeration

of the nanoparticles and thus minimized the loss of the active surface area.

In another study, 2D ultrathin Pd nanosheets were facilely prepared by one-pot reduction of $Pd(acac)_2$ in formic acid with trioctylphosphine oxide (TOPO) and cetyltrimethylammonium bromide (CTAB) at 30 °C for 24 h, and used for EOR electrocatalysis [65]. TEM study (Fig. 2b) clearly shows the formation of a planar nanostructure with some wrinkles and curls, which possesses a large specific surface area. X−ray diffraction (XRD) measurements (Fig. 2c) suggested that the formation of nanosheets was due to the preferential growth of the ⟨111⟩ planes with CO as the reducing agent; and voltammetric measurements showed a markedly enhanced electrochemical surface area of the Pd nanosheets (ECSA, 234 m^2 g^{-1}), as compared to that of commercial Pd black (68 m^2 g^{-1}). Notably, the electrocatalytic activity towards EOR was found to increase by about 1.8 folds, most likely due to the exposure of abundant surface atoms.

In a separate study, Slabon and co-workers prepared 2D arrays of Au nanocrystals (8.0 $\pm$ 1.0 nm in diameter) by one-pot reduction of gold (III) acetate with OAm and 1,2-hexadecanediol at 30 °C for 24 h, and observed excellent electrocatalytic activity towards MOR and EOR [66]. The oxidation peak current density was found to be 49 and 74 μA cm^{-2} in 0.1 and 1.0 M KOH along with 1.0 M methanol, respectively. The corresponding mass activity in the 1.0 M KOH + 1.0 M ethanol solution was estimated to be 830 A g^{-1}. Song et al. prepared 2D circular Pt nanodendrites with a mean size of 138.8 $\pm$ 25.3 nm and thickness of 13.4 $\pm$ 4.7 nm (Fig. 2d) by chemical reduction of platinum complexes with ascorbic acid in the presence of a P123 block copolymer and preformed seeds, which exhibited a much larger ECSA of 43.4 $\pm$ 0.2 m^2 g^{-1} than commercial Pt black (23.5 $\pm$ 1.4 m^2 g^{-1}), and the peak current density towards MOR was 1.4 times that of Pt black [67].

In recent studies, Chen and coworkers also observed apparent electrocatalytic activities of 2D nanostructures of Rh towards MOR [68-73]. Experimentally, ultrathin 2D hierarchical porous Rh nanosheets were prepared by a facile hydrothermal method mediated by 1-hydroxyethylidene and 1,1-diphosphonic acid (HEDP) [68]. Owing to the coordination interaction between HEDP and Rh^{3+} and the water solubility of HEDP, the as-prepared Rh nanosheets exhibited an ultralow thickness of about 1.7 nm, abundant pores/edge atoms (Fig. 2e), and grain boundary atoms. These unique structural characteristics facilitated electron transport, mass transfer, and accessibility of active sites for MOR. Indeed, in comparison to commercial Rh black, the porous Rh nanosheets possessed a larger ECSA (73.13 m^2 g^{-1} *vs.* 42.04 m^2 g^{-1}), a smaller charge transfer resistance (R_{CT}, 10 Ω *vs.* 20 Ω), and a higher specific activity (333 A g_{Rh}^{-1} *vs.* 99.5 A g_{Rh}^{-1}) (Fig. 2f). Consistent results were obtained in theoretical calculations, which showed a larger methanol adsorption energy and lower energy barrier in MOR by the Rh nanosheets.

In another study [69], Chen and coworkers prepared nanocomposites consisting of Rh nanosheets and reduced graphene oxide (RGO) as effective electrocatalysts for MOR. In the synthetic process, polyethylenimine (PEI, M_w = 600) was used as the stabilizing and facet-selective agent to facilitate the growth of sheet-like nanostructures, due to the strong adsorption of amine groups onto the Rh(111) facets (Fig. 2g). The thickness of the Rh nanosheet-RGO nanocomposites was estimated to be ca. 3 nm by AFM measurements, where the RGO facilitated the formation and stabilization of the Rh nanosheets. In electrochemical measurements, the Rh nanosheet-RGO nanocomposites were found to deliver a specific current density of 264 A g_{Rh}^{-1}, as compared to only 171 A g_{Rh}^{-1} for Rh nanoparticle-RGO and 73 A g_{Rh}^{-1} for Rh nanoparticles alone. This was ascribed to the markedly increased number of active sites in the 2D nanostructures, as compared to the nanoparticle form.

The activity can be further enhanced by a precise control of the morphology and porosity of the ultrathin 2D nanosheets. Recently, Hong et al. fabricated 2D ultrathin Pd nanomeshes by oxidizing initially
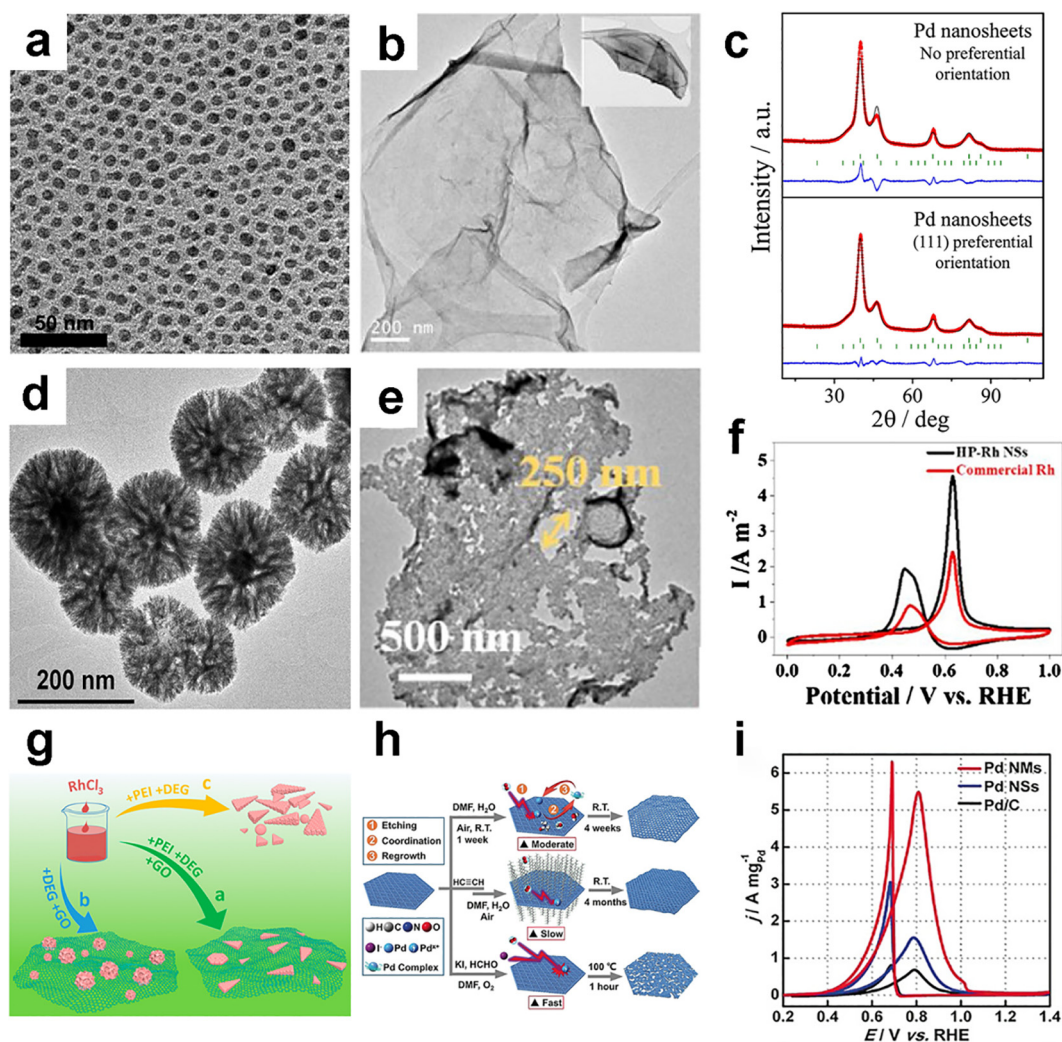
Fig. 2. (a) TEM image of a self-assembled Pd nanocrystal array. (b) Representative TEM image of Pd nanosheets showing a flat morphology and, less frequently, a curved shape (see inset). (c) XRD patterns of Pd nanosheets without any preferential orientation and oriented preferentially along the ⟨111⟩ direction. (d) TEM image of Pt nanostructures prepared an in aqueous solution of 0.067 mM P123. (e) TEM image of hierarchical porous Rh nanosheets. (f) ECSA-normalized CV curves of hierarchical porous Rh nanosheets and commercial Rh black recorded in N_2-saturated 1 M KOH + 0.5 M methanol solution at the scan rate of 50 mV s^{-1}. (g) Synthesis process of Rh nanosheets/RGO hybrids, Rh nanoparticles/RGO hybrids, and Rh nanoparticles. (h) Schematic representation of the formation process of Pd nanomeshes. (i) CV curves of ultrathin Pd nanomeshes, ultrathin Pd nanosheets, and commercial Pd/C in 1 M KOH + 1 M ethanol at the scan rate of 50 mV s^{-1}. (a) Reprinted from Ref. [64], Copyright (2016), with permission from Elsevier. (b, c) Reprinted from Ref. [65], Copyright (2018), with permission from Elsevier. (d) Reprinted from Ref. [67], Copyright (2018), with permission from Elsevier. (e, f) Reprinted from Ref. [68], Copyright (2019), with permission from Elsevier. (g) Reprinted with permission from Ref. [69]. Copyright (2017) American Chemical Society. (h, i) Reprinted with permission from Ref. [74], Copyright (2018) Wiley-VCH.

solid Pd nanosheets with air or pure O_2, where the porosity can be controlled by adjusting the oxidative etching intensity and time (Fig. 2h) [74]. The obtained ultrathin mesoporous Pd nanomeshes exhibited an average thickness of about 3 nm and pore size of 11.4 nm. Thanks to the high fraction of exposed surface atoms and active sites, the Pd nanomeshes exhibited a large ECSA of 76.1 m^2 g^{-1}, and a high peak current density of 5400 A g$_{Pd}^{-1}$ (7.09 mA cm^{-2}), in comparison to the pristine Pd nanosheets (1490 A g$_{Pd}^{-1}$, 3.42 mA cm^{-2}) and commercial Pd/C (670 A g$_{Pd}^{-1}$, 2.54 mA cm^{-2}) (Fig. 2i).

In these studies, one can see that 2D noble metal nanostructures display a superior electrocatalytic performance towards MOR/EOR, as compared to the bulk and nanoparticle counterparts, due to preferential exposure of select crystalline planes, rich active sites on the surface, large active area, shortened electron/ion migration path, and good structural stability.

2.2. Metal alloys

As mentioned above, the performance of alcohol electrooxidation can be further enhanced by alloying noble metal catalysts with another oxyphilic metal (e.g., Ru for MOR and Sn for EOR). This is primarily to mitigate the issue of self-poisoning of the catalysts by the strongly adsorbed CO_{ads}−like intermediates [48,75]. A third co-catalyst has also been added to deepen the oxidation of more complicated alcohols, such as W, Ni, Ir, and some rare-earth metals by taking advantage of their unique 4f electronic configurations to facilitate the cleavage of the C−C bond, leading to enhanced electrocatalytic activity and durability [75,76].

As shown in Fig. 3a, Gao et al. prepared an ensemble of ultrathin 2D nanosheets of Pd−based binary alloys by a universal surfactant-free strategy and observed a high performance towards alcohol oxidation [77]. A series of Pd−M (M = Ag, Pb, Au, Ga, Cu, Pt, etc.) alloy nanosheets were facilely obtained with a similar tremella-like morphology
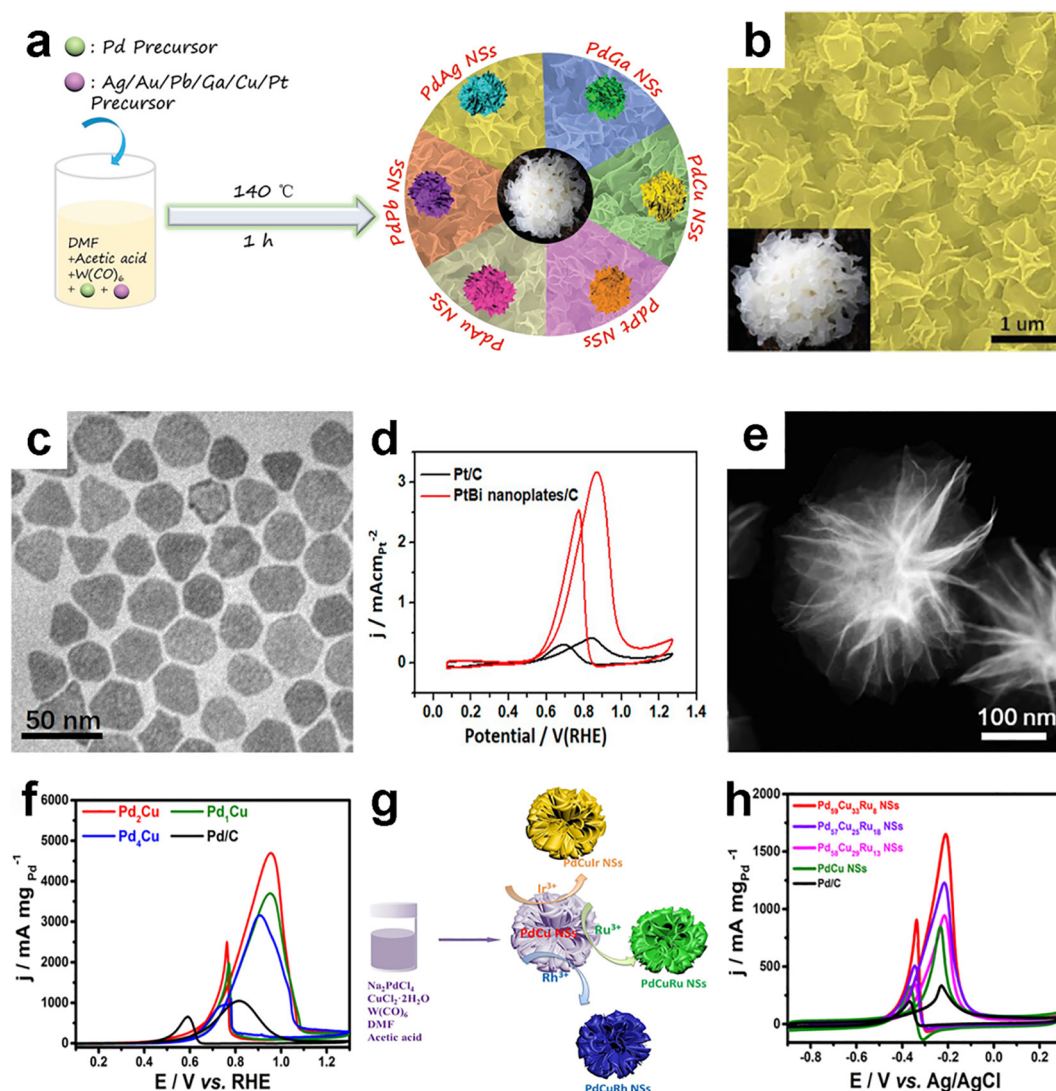
Fig. 3. (a) Schematic illustration of the synthesis of 3D tremella-like Pd–M (M = Ag, Au, Pb, Ga, Cu, and Pt) nanosheets. (b) Representative SEM image of as-prepared Pd$_7$Ag nanosheets (inset is a photograph of real tremella). (c) TEM image of PtBi/Pt core/shell nanoplates. (d) ECSA-normalized CVs of PtBi nanoplate/C and commercial Pt/C recorded in 0.1 M HClO$_4$ + 0.1 M MeOH. (e) High-angle annular dark field-scanning transmission electron microscopy (HAADF-STEM) image of Pd$_2$Cu nanoflowers. (f) CV curves of Pd$_2$Cu, Pd$_1$Cu, Pd$_4$Cu nanoflowers, and Pd/C catalysts in 1 M KOH + 1 M ethylene glycol. (g) Schematic illustration of the synthetic process of 3D PdCuM (M = Ru, Rh, Ir) alloy nanosheets. (h) CV curves of different electrocatalysts in 1 M KOH + 1 M CH$_3$OH at the scan rate of 50 mV s^{-1}. (a, b) Reprinted with permission from Ref. [77]. Copyright (2020) Wiley-VCH. (c, d) Reprinted with permission from Ref. [78]. Copyright (2018) American Chemical Society. (e, f) Reprinted from Ref. [79], Copyright (2019), with permission from Elsevier. (g, h) Reprinted with permission from Ref. [80]. Copyright (2019) American Chemical Society.

(Fig. 3b). Among the samples, Pd$_7$Ag nanosheets displayed the highest electrocatalytic activity of 2180 A g^{-1} (4.4 mA cm^{-2}) for MOR, 7080 A g^{-1} (14.3 mA cm^{-2}) for EOR, and 7010 A g^{-1} (14.1 mA cm^{-2}) for ethylene glycol oxidation reaction (EGOR) in a solution containing 0.5 M KOH and 1.0 M alcohol. In addition, the Pd$_7$Ag nanosheets showed the lowest activity decay with a 66.8% loss after 3600 s at + 0.8 V vs. RHE and a 45.8% loss after 500 successive cycles.

In another study [78], Guo et al. synthesized 2D hexagonal PtBi/Pt core–shell nanoplates by reducing Pd(acac)$_2$ and Bi(OAc)$_3$ with L-as-corbic acid and NH$_4$Br in 1-octadecene and OAm at 160 °C for 5 h, and observed exceptional bifunctional electrocatalytic activity towards both ORR and MOR. The thickness of the nanoplates could be controlled by the reaction time, for instance, 9.5 nm at 30 min and 29.0 nm at 5 h (Fig. 3c). The electrocatalytic performance was then tested by cyclic voltammetric (CV) measurements in 0.1 M HClO$_4$ + 0.1 M methanol. The PtBi/Pt core–shell nanoplates exhibited a high specific activity of 3.18 mA cm^{-2} and mass activity of 1100 A g^{-1}, as compared to

0.430 mA cm^{-2} and 300 A g^{-1} for commercial Pt/C (Fig. 3d). The nanoplates also displayed markedly enhanced stability. This remark-able performance was ascribed to the core–shell structure composed of an intermetallic hcp PtBi core and an ultrathin fcc Pt shell, which also endowed high durability to the PtBi nanoplates.

Separately, Du et al. fabricated 3D PdCu alloy nanoflowers con-sisting of ultrathin 2D nanosheets (Fig. 3e) by the reduction of Na$_2$PdCl$_4$, CuCl$_2$·2H$_2$O, and W(CO)$_6$ in a mixture of N,N-di-methylformamide (DMF) and acetic acid at 150 °C for 3 h in an oil bath, which exhibited apparent electrocatalytic activity towards EGOR [79]. Among the series of alloys, the Pd$_2$Cu nanoflowers delivered the highest mass activity of 4714.1 A g^{-1} for EGOR in 1 M KOH + 1 M ethylene glycol (Fig. 3f). In chronoamperometric (CA) test for 3600 s, the current density remained much higher than those of other PdCu alloys and commercial Pd/C.

In a similar procedure, Jin and coworkers synthesized PdCuM (M = Ru, Rh, and Ir) ternary alloy nanosheets (Fig. 3g) by the

reduction of Na_2PdCl_4, $CuCl_2·2H_2O$, and $W(CO)_6$ in a mixture of DMF and acetic acid [80]. The thickness of the ultrathin nanosheets was estimated to be as low as 2.8 nm. CV tests in 1 M KOH showed that the ECSA values of $Pd_{59}Cu_{33}Ru_8$, $Pd_{58}Cu_{29}Ru_{13}$, $Pd_{58}Cu_{29}Ru_{18}$, PdCu, and commercial Pd/C nanosheets were 35.3, 28.5, 31.2, 21.7, and 20.2 m^2 g^{-1}, respectively. Among these, $Pd_{59}Cu_{33}Ru_8$ exhibited the highest mass specific activity of 1660 A g^{-1} (4.7 mA cm^{-2}) in 1 M KOH + 1 M methanol (Fig. 3h), in comparison to 1180 A g^{-1} for $Pd_{63}Cu_{29}Rh_8$ and 1550 A g^{-1} for $Pd_{57}Cu_{34}Ir_9$. This was accounted for by the abundant channels for fast mass transport, and ligand effect of M on the PdCu electrocatalytic performance for MOR.

Cao et al. reported the synthesis of quasi-2D PdCu bimetallic trigonal hierarchical nanoframes (THNFs) based on ascorbic acid reduction of Cu^{2+} and Cu seed-mediated growth of Pd [81]. Among the obtained binary alloys, $Pd_{5.89}Cu$ was found to deliver the highest mass activity of 4520 A g^{-1}, and $Pd_{8.57}Cu$ had the largest specific activity of 5.94 mA cm^{-2}. The ECSA values of most of the THNFs were larger (108.6 m^2·g$_{Pd}^{-1}$) than that of commercial Pd black, suggesting a high degree of Pd utilization.

Xu and coworkers prepared a heterostructure consisting of 2D NiZn oxyphosphide nanosheets and 3D PdRu nanoflowers by a facile wet-chemistry strategy using $NaBH_4$ as the reducing agent and polyvinylpyrrolidone (PVP) as the protecting agent [54]. From the TEM image in Fig. 4a, one can see that the PdRu alloy nanoflowers consisted of interconnected nanosheets grown on the NiZn oxyphosphide nanosheet surface. In 1 M KOH + 1 M methanol or ethanol, the heterostructure delivered a specific/mass activity of 4.5 mA cm^{-2}/1739.5 A g^{-1} for MOR (Fig. 4b) and 12.3 mA cm^{-2}/4719.8 A g^{-1} for EOR (Fig. 4c), respectively. The incorporation of NiZn oxyphosphide nanosheets enhanced the cycling stability as well as electrocatalytic activity, where the poisoning resistance resulted from its ability of water dissolution that facilitated the recovery of poisoned electrocatalysts. The retention rate of the specific/mass activities reached > 70% after 1000 successive cycles (Fig. 4d and 4e).

2D PtSn nanosheets (sub-1 nm thickness) were prepared by Tuan's group through a facile colloidal method and used as effective electrocatalysts for both MOR and EOR [55]. AFM and high-resolution TEM measurements showed that the thickness ranged from 0.6 to 0.9 nm. With surfactants controlling the growth of six facet directions, stacked hexagonal nanostructures were formed, as evidenced in SEM measurements (Fig. 4f). Electrochemically, the obtained PtSn nanosheets exhibited a mass activity towards MOR (871.6 A g$_{Pt}^{-1}$) 2.3 times (371 A g$_{Pt}^{-1}$) and 10.1 times (86.1 A g$_{Pt}^{-1}$) higher than that of commercial Pt/C and Pt black, respectively, and a mass activity towards EOR (673.6 A g$_{Pt}^{-1}$) 5.3 and 2.3 times higher than those of commercial Pt/C (295 A g$_{Pt}^{-1}$) and Pt black (127.7 A g$_{Pt}^{-1}$), respectively.
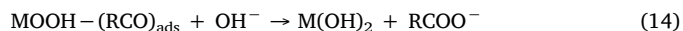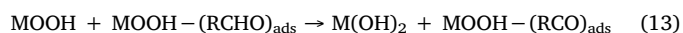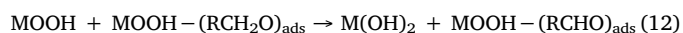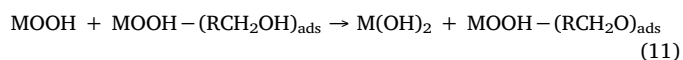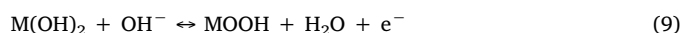
Lv et al. used a surfactant template, docosyltrimethylammonium chloride, to prepare ultrathin, free-standing trimetallic PdPtCu nanosheets with ascorbic acid as the reducing agent [82]. The surfactant facilitated the formation of a lamellar nanostructure, which exhibited linear voids after the removal of the surfactant (Fig. 4g). From the CV curves in Fig. 4h, the PdPtCu nanosheets were found to exhibit an ECSA of 46.3 m^2 g^{-1}, as compared to 20.9 m^2 g^{-1} of PdPt nanosheets, 30.1 m^2 g^{-1} of PdCu nanosheets, and 19.4 m^2 g^{-1} of monometallic Pd nanosheets, and apparent electrocatalytic activity towards the oxidation of methanol, ethanol, glycerol, and glucose.

Wang's group used Ag triangular nanoplates to prepare 2D porous PtAg alloy nanosheets through a galvanic replacement reaction [83]. Because ascorbic acid was used as the reducing agent, excessive oxidative corrosion of the Ag triangular nanoplates was avoided and the nanoplate morphologies were retained (Fig. 4i). In the solution of 1 M KOH + 1 M methanol, the PtAg porous nanosheets achieved a specific anodic current density of 10.04 mA cm^{-2}, which was 4.5 times that of commercial Pt/C (2.24 mA cm^{-2}). The PtAg nanosheets also exhibited remarkable stability, retaining 19.4% of the current density (1.95 mA cm^{-2}) after continuous operation for 5000 s, in comparison

to almost complete loss with Pt/C. The remarkable activity was ascribed to the unique 2D porous architectures that featured plenty of catalytically active sites for effective electron and mass transport. The AOR performances of these different 2D noble metals and alloys are summarized in Table 1.

3. Metal oxides and hydroxides

Due to their excellent physical and electrochemical properties, transition metal oxides and hydroxides have emerged as viable substitutes for precious metals towards the electrocatalytic oxidation of alcohols [84-87]. Several important parameters need to be considered, such as high structural stability, high resistance against electrochemical corrosion, good electrical and proton conductivity, and high specific surface area. Among these, 2D nanosheets of transition metal oxides and hydroxides, such as NiO, spinel nickel cobaltate ($NiCo_2O_4$), and LDHs, have been attracting much attention. Generally, alkaline electrolytes are preferred for transition metal oxides and hydroxides, because the catalysts are more stable in alkaline electrolyte than in acidic media. The possible pathways of AOR on divalent metal oxides and hydroxides (such as cobalt- and nickel-based electrocatalysts) are listed below [88-90], in which the trivalent oxyhydroxide MOOH serves as the adsorption sites and oxidants for AOR,

$$MO + OH^- \leftrightarrow MOOH + e^- \tag{8}$$

$$M(OH)_2 + OH^- \leftrightarrow MOOH + H_2O + e^- \tag{9}$$

$$MOOH + RCH_2OH \leftrightarrow MOOH-(RCH_2OH)_{ads} \tag{10}$$

$$MOOH + MOOH-(RCH_2OH)_{ads} \rightarrow M(OH)_2 + MOOH-(RCH_2O)_{ads} \tag{11}$$

$$MOOH + MOOH-(RCH_2O)_{ads} \rightarrow M(OH)_2 + MOOH-(RCHO)_{ads} \tag{12}$$

$$MOOH + MOOH-(RCHO)_{ads} \rightarrow M(OH)_2 + MOOH-(RCO)_{ads} \tag{13}$$

$$MOOH-(RCO)_{ads} + OH^- \rightarrow M(OH)_2 + RCOO^- \tag{14}$$

3.1. Transition metal oxides

A range of transition metal oxides have been found to exhibit electrocatalytic activity towards AOR. For instance, NiO is an attractive candidate, where the main limiting factors are its poor electrical conductivity and low utilization rate as electrode materials [91]. Preparation of 2D sheet-like nanostructures can improve the effective utilization of the active materials and at the same time create abundant oxygen vacancies on their surfaces, leading to an increase of the defect states in the forbidden band and thus improved electrical conductivity. For instance, Luo et al. prepared 2D ultrathin NiO nanosheets with rich oxygen vacancies (V_O-rich ultrathin NiO nanosheets) through a facile hydrothermal and calcination procedure [92]. For comparison, they also prepared NiO nanosheets poor in oxygen vacancies (V_O-poor ultrathin NiO nanosheets) by prolonged calcination, and bulk NiO by direct high-temperature calcination of $Ni(NO_3)_2·6H_2O$ (Fig. 5a). The V_O-rich nanosheets achieved a large current density of 85.3 mA cm^{-2} towards MOR, more than twice that (36.9 mA cm^{-2}) of the V_O-poor counterpart and almost four times that (23.9 mA cm^{-2}) of bulk NiO (Fig. 5b), along with improved catalytic stability. Results based on density functional theory (DFT) calculations showed that the formation of abundant oxygen vacancies indeed decreased the band gap and increased the electrical conductivity.

$NiCo_2O_4$ is another attractive material [93,94]. For instance, Xiao's group prepared $NiCo_2O_4$ nanospheres by the assembly of porous nanosheets [95]. From the TEM image in Fig. 5c, one can see that the $NiCo_2O_4$ nanospheres exhibited a wrinkled, porous structure consisting of numerous stacked nanoparticles. From nitrogen adsorption and desorption measurements, the BET specific surface area was estimated
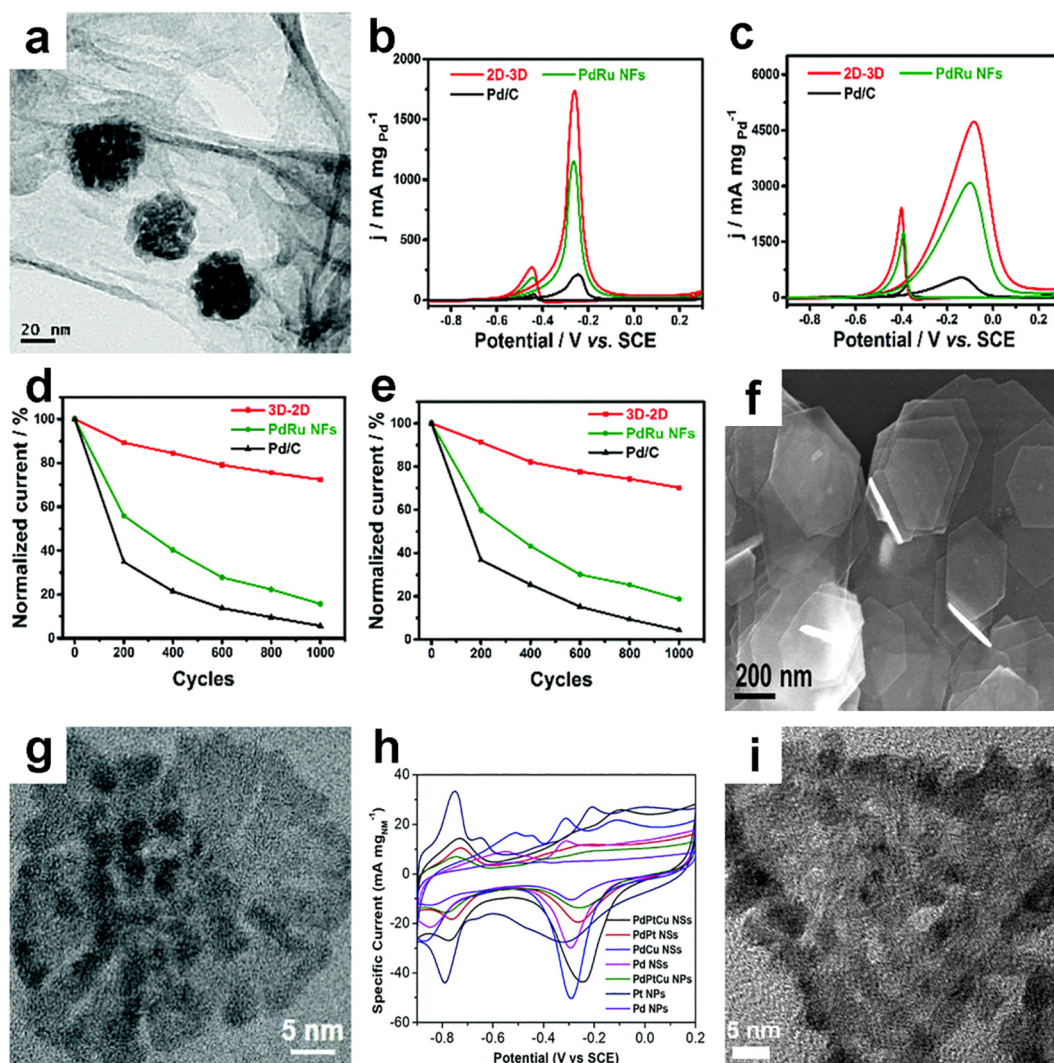
Fig. 4. (a) TEM image of $3D-2D$ PdRu/NiZn oxyphosphide nanohybrids. CV curves of $3D-2D$ nanohybrids, 3D PdRu NFs, and Pd/C in (b) 1 M KOH + 1 M CH_3OH, and (c) 1 M KOH + 1 M CH_3CH_2OH at the scan rate of 50 mV s^{-1}. Long-term stability comparison of $3D-2D$ nanohybrids, 3D PdRu NFs, and Pd/C for 1000 potential cycles toward (d) MOR and (e) EOR. (f) SEM image of PtSn nanosheets. (g) High-magnification TEM image of the ultrathin PdPtCu nanosheets. (h) CV curves of the trimetallic PdPtCu nanosheets, bimetallic PdPt and PdCu nanosheets, monometallic Pd nanosheets, PdPtCu nanoparticles, and commercial Pt and Pd nanoparticles in 1.0 M KOH at 50 mV s^{-1}. (i) Typical TEM image of porous PtAg nanosheets. (a-e) Reproduced from Ref. [54] with permission from The Royal Society of Chemistry. (f) Reprinted from Ref. [55], Copyright (2018), with permission from Elsevier. (g, h) Reproduced from Ref. [82] with permission from The Royal Society of Chemistry. (i) Reprinted from Ref. [83], Copyright (2018) Springer Nature.

to be 146.5 $m^2 g^{-1}$. The nickel foam-supported electrode ($NiCo_2O_4$/NF) exhibited a current density of 40.9 A g^{-1} in 1 M KOH + 0.5 M methanol, about an order of magnitude higher than the background current of 4.6 A g^{-1} in 1 M KOH. Furthermore, the $NiCo_2O_4$/NF electrode exhibited a negligible decrease in current density in long-term stability and durability tests for MOR.

3.2. Transition metal hydroxides

Transition metal hydroxides, including layered single metal hydroxides and LDHs, have a typical open layered, 2D structure with an easily adjustable interlayer distance [96,97]. LDHs with the general formula of $M_{1-x}^{2+}M_x^{3+}(OH)_2^{2-}A_{x/n}^{n-}\cdot mH_2O$ and a diverse chemical composition have also been used in the electrocatalysis of AOR [16,98–100]. For instance, Chen et al. prepared 2D ultrathin NiAl−LDHs nanosheets by a simple hydrothermal and mechanical liquid-exfoliation method [90]. AFM measurements (Fig. 5d) showed that the exfoliated nanosheets consisted of single or double layers, with the thickness ranging from 0.75 to 0.88 nm. In electrochemical measurements for EOR in 1.0 M NaOH and

1.0 M ethanol, the oxidation current density of NiAl−LDHs nanosheets (543.33 A g^{-1}) at + 0.58 V *vs.* Ag/AgCl was 39 times higher than that of bulk NiAl−LDHs (13.65 A g^{-1}) (Fig. 5e); and 91.6% and 81.8% of its initial current density was retained after continuous operation at + 0.58 V *vs.* Ag/AgCl for 2000 s and 10000 s, which is much better than that of bulk NiAl−LDHs. The ultrathin LDH nanosheets allowed for the exposure of a great number of active sites. More importantly, exfoliation led to the formation of Ni(III) active species (NiOOH) on the nanosheets, which played a critical role in determining the catalytic activity towards EOR. The NiOOH also improved the electrical conductivity of the LDH nanosheets. These effects synergistically led to marked enhancement of the EOR activity, as compared to bulk NiAl−LDHs.

In another study [101], Hou's group synthesized Mn−doped Ni(OH)$_2$ nanosheets by mixing Mn(OH)$_2$ nanoplates with Ni^{2+} (Fig. 5f). As the solubility product of Ni(OH)$_2$ is lower than that of Mn(OH)$_2$, the Mn(OH)$_2$ templates were sacrificed to introduce Ni^{2+} as the dopant, and the doped sample was found to exhibit a larger peak current density (Fig. 5g) and better cyclic stability than the pristine one toward EOR.

Table 1
Comparison of the alcohol oxidation performances with different 2D noble metals and alloys as electrocatalysts.

| Electrocatalyst	Electrolyte		Peak current density from CV curves	ECSA (m² g⁻¹)	Ref.
Pd nanocrystal arrays	Alkaline medium	0.5 M NaOH and 1.0 M alcohol	1040 mA mg^{-1}, 6.7 mA cm^{-2} at 50 mV s^{-1} for MOR; 5500 mA mg^{-1}, 35.7 mA cm^{-2} at 50 mV s^{-1} for EOR	12.10	[64]
Pd nanosheets		0.1 M KOH and 0.5 M ethanol	150 mA g^{-1} vs. Pd-black (30 mA g^{-1}) at 10 mV s^{-1}	194 (53 for Pd-black)	[65]
Au nanocrystal arrays		1.0 M KOH and 1.0 M alcohol	48.3 mA mg^{-1} at 50 mV s^{-1} for MOR; 830 mA mg^{-1} at 50 mV s^{-1} for EOR	65.84	[66]
Ultrathin porous Rh nanosheets		1.0 M KOH and 0.5 M methanol	333 mA mg^{-1}, 0.455 mA cm^{-2} vs. Rh balck (99.5 mA mg^{-1}, 0.237 mA cm^{-2}) at 50 mV s^{-1}	73.13 (42.04 for Rh-black)	[68]
Rh nanosheets/RGO hybrids		1.0 M KOH and 1.0 M methanol	264 mA mg^{-1} vs. Pt/C (73 mA mg^{-1}) at 50 mV s^{-1}	48.66 (51.04 for Pt/C)	[69]
Ultrathin Pd nanomeshes		1.0 M KOH and 1.0 M ethanol	5400 mA mg^{-1}, 7.09 mA cm^{-2} vs. Pt/C (670 mA mg^{-1}, 2.54 mA cm^{-2}) at 50 mV s^{-1}	76.1 (26.4 for Pd/C)	[74]
Pd₇Ag nanosheet		0.5 M KOH and 1.0 M alcohol	2180 mA mg^{-1}, 4.4 mA cm^{-2} vs. Pd/C (410 mA mg^{-1}, 1.0 mA cm^{-2}) for MOR; 7080 mA mg^{-1}, 14.3 mA cm^{-2} vs. Pd/C (860 mA mg^{-1}, 2.2 mA cm^{-2}) for EOR; 7010 mA mg^{-1}, 14.1 mA cm^{-2} vs. Pd/C (960 mA mg^{-1}, 2.4 mA cm^{-2}) for EGOR	49.6 (39.0 for Pd/C)	[77]
Pd₂Cu nanosheets-constructed nanoflowers		1.0 M KOH and 1.0 M ethylene glycol	4714.1 mA mg^{-1}, 13.7 mA cm^{-2} vs. Pd/C (1066.8 mA mg^{-1}, 2.0 mA cm^{-2}) at 50 mV s^{-1}	34.6 (53.1 for Pd/C)	[79]
Pd₅₉Cu₃₃Ru₈ nanosheets		1.0 M KOH and 1.0 M methanol	1660.8 mA mg^{-1}, 4.7 mA cm^{-2} vs. Pd/C (338.9 mA mg^{-1}, 1.68 mA cm^{-2}) at 50 mV s^{-1}	35.3 (20.2 for Pd/C)	[80]
Pd₅.₈₉Cu/Pd₈.₅₇Cu trigonal hierarchical nanoframes		1.0 M KOH and 1.0 M ethanol	4520 mA mg^{-1}, 5.94 mA cm^{-2} vs. Pd-black (660 mA mg^{-1}, 0.61 mA cm^{-2}) at 50 mV s^{-1}	104/76 (108.6 for Pd-balck)	[81]
PdRu nanosheets		1.0 M KOH and 1.0 M alcohol	1739.5 mA mg^{-1}, 4.5 mA cm^{-2} vs. Pd/C (209.3 mA mg^{-1}, 0.5 mA cm^{-2}) at 50 mV s^{-1} for MOR; 4719.8 mA mg^{-1}, 12.3 mA cm^{-2} vs. Pd/C (569.7 mA mg^{-1}, 1.3 mA cm^{-2}) at 50 mV s^{-1} for EOR	34.3 (42.6 for Pd/C)	[54]
PtSn ultrathin sheets		0.2 M KOH and 0.2 M alcohol	876.1 mA mg^{-1}, 15.86 mA cm^{-2} vs. Pt/C (371 mA mg^{-1}, 4.04 mA cm^{-2}), Pt-black (86.1 mA mg^{-1}, 4.39 mA cm^{-2}) at 50 mV s^{-1} for MOR; 673.6 mA mg^{-1}, 24.5 mA cm^{-2} vs. Pt/C (295 mA mg^{-1}, 6.0 mA cm^{-2}), Pt-black (127.7 mA mg^{-1}, 13.0 mA cm^{-2}) at 50 mV s^{-1} for EOR	66 (28.6 for Pt/C and 24.8 for Pt-black)	[55]
Ultrathin PdPtCu nanosheets		1.0 M KOH and 1.0 M methanol	2670 mA mg^{-1} vs. Pd nanoparticles (1430 mA mg^{-1}), Pt nanoparticles (470 mA mg^{-1}) at 50 mV s^{-1}	46.3 (10.0 for PdPtCu nanoparticles)	[82]
PtAg porous nanosheets		1.0 M KOH and 1.0 M methanol	3990 mA mg^{-1}, 10.04 mA cm^{-2} vs. Pt/C (1490 mA mg^{-1}, 2.24 mA cm^{-2}) at 50 mV s^{-1}	39.8 (66.7 for Pt/C)	[83]
Circular Pt nanodendrites	Acidic medium	0.5 M H₂SO₄ and 1.0 M methanol	~28 mA cm^{-2} vs. Pt-black (~20 mA cm^{-2}) at 20 mV s^{-1}	43.4 (23.5 for Pt-balck)	[67]
PtBi/Pt core–shell nanoplates		0.1 M HClO₄ and 0.1 M methanol	1100 mA mg^{-1}, 3.18 mA cm^{-2} vs. Pt/C (300 mA mg^{-1}, 0.43 mA cm^{-2}) at 50 mV s^{-1}	33.9 (71.34 for Pt/C)	[78]

8
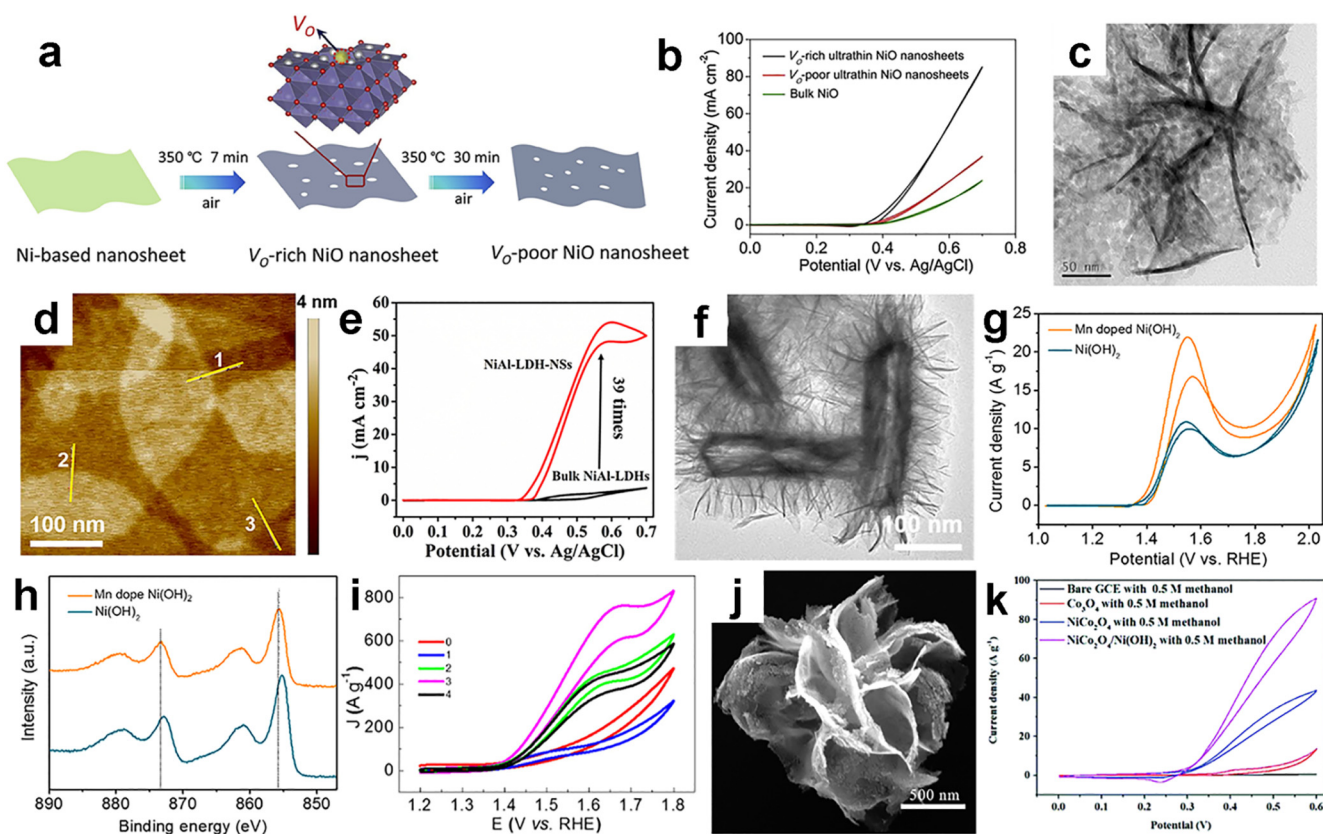
Fig. 5. (a) Schematic illustration for the fabrication of V_O-rich/poor ultrathin NiO nanosheets. (b) CV curves of the various NiO samples in 1 M KOH + 0.5 M CH$_3$OH. (c) TEM image of NiCo$_2$O$_4$. (d) AFM topograph of NiAl−LDH nanosheets. (e) CV curves of bulk NiAl−LDHs and NiAl−LDH nanosheets modified electrodes in 1.0 M NaOH + 1.0 M ethanol at the scan rate of 50 mV s^{-1}. (f) TEM image of the hollow Mn-doped Ni(OH)$_2$ nanostructures. (g) CVs of hollow Mn-doped Ni(OH)$_2$ nanostructures and Ni(OH)$_2$ nanosheets modified electrode in 1 M KOH + 0.5 M CH$_3$OH at the scan rate of 50 mV s^{-1}. (h) XPS spectra of Ni 2p electrons of hollow Mn-doped Ni(OH)$_2$ nanostructures and Ni(OH)$_2$ nanosheets. (i) CV curves in nitrogen-saturated 1 M KOH + 3 M CH$_3$OH. (j) FESEM image of NiCo$_2$O$_4$/Ni(OH)$_2$. (k) CV curves of GCE (black), Co$_3$O$_4$/GCE (red), NiCo$_2$O$_4$/GCE (blue), and NiCo$_2$O$_4$/Ni(OH)$_2$/GCE (magenta) in 1 M KOH + 0.5 M CH$_3$OH at the scan rate of 10 mV s^{-1}. (a, b) Reprinted from Ref. [92], Copyright (2018), with permission from Elsevier. (c) Reprinted from Ref. [95], Copyright (2014), with permission from Elsevier. (d, e) Reprinted from Ref. [90], Copyright (2017), with permission from Elsevier. (f-h) Reprinted from Ref. [101], Copyright (2018), with permission from Elsevier. (i) Reprinted with permission from Ref. [102]. Copyright (2018) American Chemical Society. (j, k) Reproduced from Ref. [103] with permission from The Royal Society of Chemistry.

XPS studies (Fig. 5h) showed that the prepared sample exhibited a higher binding energy of the Ni 2p$_{3/2}$ electrons than that of undoped Ni(OH)$_2$, which was beneficial to increase the number of nickel active species and hence the electrocatalytic activity.

3.3. Metal oxide − hydroxide hybrids

Compared with transition metal oxides or hydroxides, 2D metal oxide-hydroxide hybrids show enhanced electrochemical performance, due to their rich composition, synergistic effect between ions, and high electrical conductivity. For instance, Chen and colleagues fabricated composites based on CuO nanoparticles supported on Co(OH)$_2$ ultrathin nanosheets as efficient electrocatalysts for MOR and investigated the influence of the amount of Cu on the electrocatalytic performance [102]. The as-obtained sample at the Cu/Co molar ratio of 1:2 (sample 3) delivered the best electrocatalytic performance among the series. At the potential of +1.65 V vs. RHE, sample 3 exhibited the highest peak current density of 764 A g^{-1} (159 mA cm^{-2}) in the electrolyte solution of 1 M KOH + 3 M methanol (Fig. 5i). In addition, sample 3 exhibited the largest turn-over frequency of 2.55 s^{-1}, a lowest Tafel slope of 92 mV dec^{-1}, and best electrochemical stability (only 30% loss in 1000 cycles). The enhanced performance was attributed to the formation of [Co(OH)$_2$]$^+$ species that led to enhanced binding energy of Co and O.

Similarly, Wang et al. synthesized 3D hierarchical binary metal oxide NiCo$_2$O$_4$ nanoflowers consisting of cross-linked 2D NiCo$_2$O$_4$ nanosheets decorated with nanoparticles by a facile microwave-assisted hydrothermal route, which provided a loading platform for the further growth of Ni(OH)$_2$ nanoparticles [103]. The intertwined sheet-like nanostructures were evidenced in field-emission scanning electron microscopy (FESEM) measurements (Fig. 5j). The anodic oxidation current density of the nanocomposites loaded on a glassy carbon electrode (NiCo$_2$O$_4$/Ni(OH)$_2$/GCE) was estimated to be 92.3 A g^{-1}, in comparison to the negligible current density with the GCE alone. In addition, the NiCo$_2$O$_4$/Ni(OH)$_2$/GCE exhibited the best stability among the series, where 94.6% of the initial current density was retained after refreshing the electrolyte solution (Fig. 5k). The remarkable electrocatalytic activity was ascribed to the hierarchical morphology of NiCo$_2$O$_4$ nanoflowers and the high activities of Ni(OH)$_2$.

In summary, 2D transition metal oxides, hydroxides, and their composites can be used as high-performance electrocatalysts for AOR, due to high electrochemical stability, good electrical and proton conductivity, high specific surface area, as well as rich composition, and synergistic interactions between the ions.

4. Metal carbides

Transition metal carbides (M$_x$C$_y$) [33], in particular, tungsten carbide, display Pt−like catalytic behaviors, and are viewed as promising catalysts to replace precious metals in DAFC [40,104-106]. However, the high density results in a small specific surface area and low
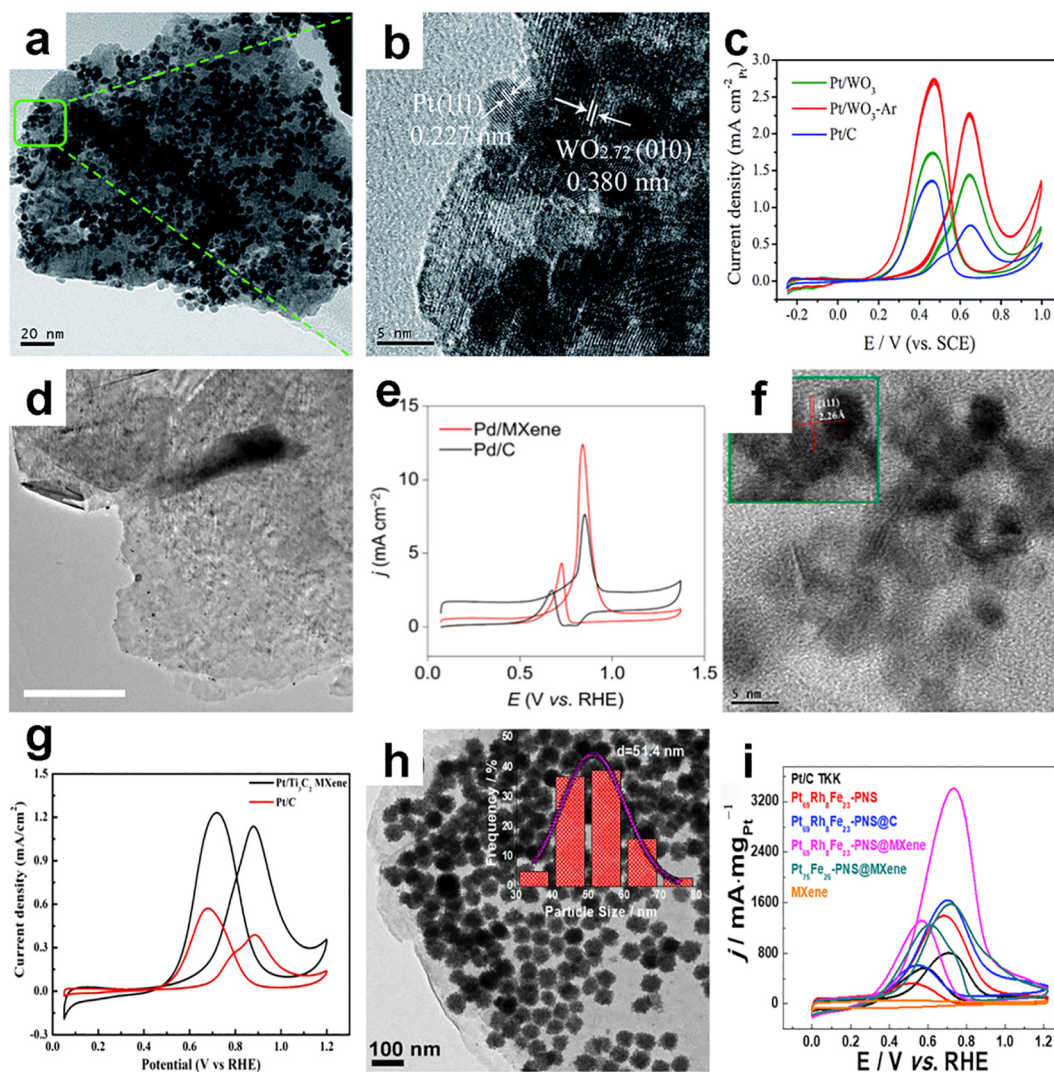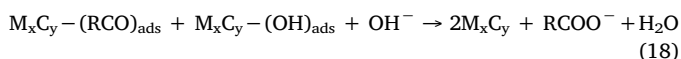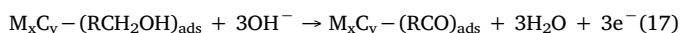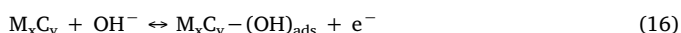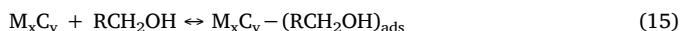
Fig. 6. (a, b) TEM images of Pt/WO₃−Ar hybrid nanostructures at different resolutions. (c) CV curves of Pt/WO₃−Ar, Pt/WO₃, and Pt/C in N₂−saturated 0.5 M H₂SO₄ + 1 M CH₃OH at the sweep rate of 50 mV s⁻¹. (d) TEM image of Pd/MXene. Scale bar is 200 nm. (e) CVs of Pd/MXene and Pd/C in a solution containing 1 M KOH and 1 M CH₃OH. (f) HRTEM image of Pt/Ti₃C₂ MXene. Inset is an image at higher magnification. (g) CV curves of Pt/Ti₃C₂ MXene and commercial Pt/C in 0.5 M H₂SO₄ + 0.5 M CH₃OH at the scan rate of 50 mV s⁻¹. (h) TEM image of porous Pt₆₉Rh₈Fe₂₃ nanosheets/MXene hybrids. Inset is the size distribution histogram of the porous trimetallic PtRhFe nanospheres. (i) CV curves of the as-prepared catalysts in N₂-saturated 1.0 M KOH + 1.0 M ethanol solution at the scan rate of 50 mV s⁻¹. (a-c) Reproduced from Ref. [121] with permission from The Royal Society of Chemistry. (d, e) Reprinted from Ref. [126]. Copyright (2019) American Chemical Society. (f, g) Reproduced from Ref. [127], Copyright (2018), with permission from Elsevier. (h, i) Reproduced from Ref. [129], Copyright (2019), with permission from Elsevier.

electrocatalytic activity, which hampers their applications in electrocatalysis. Such issues can be mitigated by using porous nanostructures of the carbide materials, because of enhanced exposure of active sites, efficient mass transport, increased release of gas bubbles, suppressed agglomeration of catalysts, and enlarged interfaces between different components. In alkaline electrolytes, the possible electrocatalytic mechanisms of AOR on transition metal carbides are listed as follows [107-109],

$$M_xC_y + RCH_2OH \leftrightarrow M_xC_y - (RCH_2OH)_{ads} \quad (15)$$

$$M_xC_y + OH^- \leftrightarrow M_xC_y - (OH)_{ads} + e^- \quad (16)$$

$$M_xC_y - (RCH_2OH)_{ads} + 3OH^- \rightarrow M_xC_y - (RCO)_{ads} + 3H_2O + 3e^- \quad (17)$$

$$M_xC_y - (RCO)_{ads} + M_xC_y - (OH)_{ads} + OH^- \rightarrow 2M_xC_y + RCOO^- + H_2O \quad (18)$$

where metal carbides provide the adsorption sites for alcohol molecules, activation of water molecules, and formation of adsorbed

surface hydroxyls [110,111]. Meanwhile, it is noteworthy that part of the metal carbides (e.g., WC and TiC) [112,113] may become corroded into the corresponding oxygenated species (WO₃ and TiO²⁺), producing OH at a relatively high potential that is critical for alcohol adsorption and CO oxidation [114].

For instance, Li et al. prepared a series of mesoporous WC nanoslices by an easy, two-step strategy that included a hydrothermal pretreatment followed by a carburization reduction process [115]. The sample prepared at 700 °C (WC₇₀₀) exhibited a specific area of 31.7 m² g⁻¹, pore size distribution in the range of 3–15 nm, and average aperture of 6.2 nm, in comparison to 9.46 m² g⁻¹, 3–60 nm and 10.0 nm for WC₇₅₀. The obtained WC nanoslices showed higher catalytic activity than both 5% and 10% Pt/C towards MOR in acidic and alkaline media.

Zheng et al. fabricated nanocrystalline WC thin films on graphite substrates by plasma-enhanced chemical vapor deposition in a H₂ and Ar atmosphere, using WF₆ and CH₄ as the precursors [116]. The resulting film electrode exhibited an ECSA of 49.3 cm², a peak current of 123.6 mA cm⁻² in the solution of 0.5 M H₂SO₄ + 2 M methanol at
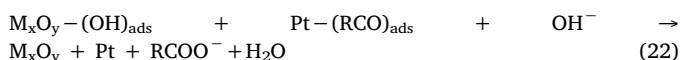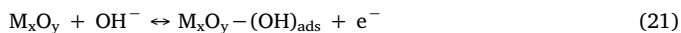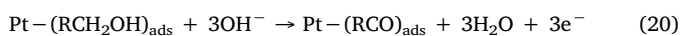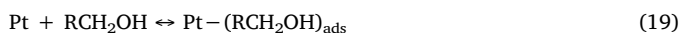
70 °C, and the oxidation peak potential of only + 0.306 V *vs.* SCE.

5. Metal−based composites

To further enhance the electrocatalytic activity of single metal oxides/hydroxides or metal carbides, a small amount of noble metals, typically Pt, can be added to form a composite [33]. In these catalysts, the 2D metal oxides and carbides usually serve as the co-catalyst and substrate support for the dispersion of the noble metals, where the synergistic interactions lead to enhanced adsorption and dissociation of alcohols.

5.1. Metal-metal oxide composites

The (noble) metal domains in the heterogeneous metal–metal oxide nanocomposites typically exhibit enhanced activity towards AOR, due to the synergistic effects between the structural components, e.g., electronic coupling and lattice strain effect. The electron donating/withdrawing effect from the metal oxide can alter the electron density around the metal sites, and thus affect their catalytic properties by changing the adsorption energy of reactants on the metal surface, leading to enhanced electrocatalytic activity and anti-toxicity [117]. The mechanism of alcohol electrooxidation catalyzed by Pt/M_xO_y nanocomposites in alkaline electrolytes is summarized below [118,119],

$$Pt + RCH_2OH \leftrightarrow Pt-(RCH_2OH)_{ads} \tag{19}$$

$$Pt-(RCH_2OH)_{ads} + 3OH^- \rightarrow Pt-(RCO)_{ads} + 3H_2O + 3e^- \tag{20}$$

$$M_xO_y + OH^- \leftrightarrow M_xO_y-(OH)_{ads} + e^- \tag{21}$$

$$M_xO_y-(OH)_{ads} + Pt-(RCO)_{ads} + OH^- \rightarrow M_xO_y + Pt + RCOO^- + H_2O \tag{22}$$

where one can see that Pt serves as the anchoring and oxidation sites for alcohols, whereas M_xO_y facilitates the formation of hydroxyl species that drives further oxidation of the Pt−adsorbed intermediates [120].

For instance, utilizing the Ar plasma exfoliation technique, Zhang and colleagues prepared Pt nanoparticles-loaded ultrathin WO_3 nanosheets, which exhibited enriched oxygen vacancies and increased electrical conductivity, as remarkable electrocatalysts towards MOR [121]. From Fig. 6a, the agglomerated Pt nanoparticles can be seen to exhibit an average particle size of 3.34 nm. After the exfoliation treatment by Ar plasma of the as-prepared bulk WO_3, oxygen-deficient WO_3 nanosheets (denoted as WO_3-Ar) were produced with the chemical formula of $WO_{2.72}$ or $W_{18}O_{49}$, as confirmed by the ⟨010⟩ planes in HRTEM measurements (Fig. 6b), which were favorable for the dispersion of Pt nanoparticles. Electrochemical measurements of Pt/WO_3-Ar in N_2-saturated 0.5 M H_2SO_4 showed that the reduction peak potential shifted positively, while the peak potential for CO stripping showed a slightly negative shift. This suggests its bifunctional roles of enhanced MOR activity and CO tolerance. The peak current density of Pt/WO_3-Ar in 0.5 M H_2SO_4 + 1 M methanol was measured to be 2.27 mA cm_{Pt}^{-2} or 1250 A g_{Pt}^{-1}, which is much higher than those of pristine Pt/WO_3 (1.44 mA cm_{Pt}^{-2} or 480 A g_{Pt}^{-1}) and Pt/C (0.77 mA cm_{Pt}^{-2} or 320 A g_{Pt}^{-1}) (Fig. 6c).

In another study, Zhang and coworkers fabricated Pt−hematene nanosheets by ultrasonic exfoliation followed by double-pulse electrodeposition. The hematene nanosheets were facilely exfoliated by a two-step ultrasonic treatment of hematite $\alpha-Fe_2O_3$ powders [122]. TEM measurements showed that the as-synthesized Pt−hematene nanosheets consisted of Pt nanoparticles with the size ranging from 8 to 10 nm. In the electrolyte solution of 1 M KOH + 1 M methanol, the peak mass activity of Pt−hematene nanosheets was estimated to be 181 mA mg^{-1}, which is lower than that (563 mA mg^{-1}) of commercial 40 wt% Pt/C but higher than those of relevant examples reported in the literature (57 mA mg^{-1} for Pt−CeO_2(1.3:1)/C, 150 mA mg^{-1} for Pt−NiO/C, and 125 mA mg^{-1} for Pt/PIN/GC). This was accounted for

by the oxophilic nature of Fe_2O_3 that improved the adsorption of OH species, leading to enhanced anti-poisoning.

5.2. Metal−metal carbide composites

In alkaline media, the electrocatalytic mechanism of AOR by metal–metal carbide composites is similar to that by metal–metal oxide composites [111,123-125]. For instance, Lang et al. prepared Pd nanoparticles loaded on 2D $Ti_3C_2T_x$ MXene based on selective etching by HF and chemical reduction by formic acid [126]. From the TEM image of Pt/MXene (Fig. 6d), one can see that a small number of Pd nanoparticles were uniformly dispersed on the ultrathin MXene nanosheets, which led to a high specific activity due to the relatively low mass loading of Pd. In the alkaline electrolyte of 1 M KOH + 1 M methanol, Pt/MXene exhibited a higher peak current density (12.4 mA cm^{-2}) than commercial Pd/C (7.6 mA cm^{-2}) (Fig. 6e). Consistent results were observed in the Tafel slopes and turnover frequencies of the catalysts, suggesting that the support of MXene indeed accelerates the reaction kinetics and thus enhances the MOR activity. More importantly, based on the results from XPS measurements and DFT calculations, it was proposed that the introduction of 2D $Ti_3C_2T_x$ MXene as the support induced strong metal-support interactions (SMSI) with the Pd nanoparticles, where electron transfer from MXene to Pd optimized the electronic structure of Pd towards methanol adsorption and oxidation. Additionally, the possible hydrogen bond formation between methanol and MXene also aided methanol adsorption and facilitated the oxidation kinetics.

In an early study, Wang et al. prepared Pt nanoparticles-decorated Ti_3C_2 MXene and observed an enhanced electrocatalytic performance towards MOR, as compared to commercial Pt/C [127]. From the TEM image of Ti_3C_2 MXene, one can see that the sample exhibited a layered structure with an interlayer spacing of about 9.8 Å. This provided abundant sites for the growth of Pt nanoparticles (4–5 nm in diameter, Fig. 6f). Electrochemical measurements showed that the ECSA of Pt/Ti_3C_2 MXene was 60.1 $m^2 g^{-1}$, much larger than that of Pt/C (30.2 $m^2 g^{-1}$). From Fig. 6g, the MOR peak current density of Pt/Ti_3C_2 MXene (1.137 mA cm^{-2}) was almost three times that of Pt/C (0.388 mA cm^{-2}). Furthermore, 85.1% of the ECSA value was retained after 1000 potential cycles from + 0.05 to + 1.2 V, in comparison to only 53.2% for Pt/C.

Chen et al. prepared a Pt/Mo_2C electrocatalyst with optimized Pt−Mo_2C chemical bonding and evaluated the EOR activity [128]. The chemical bonding of Mo_2C to Pt particles rendered exceptional EOR activity at low potentials, which was 15 and 2.5 times higher than those of Pt/C and commercial 40% PtRu/C, respectively, at + 0.6 V *vs.* RHE. The stability of the Pt/Mo_2C/C electrocatalyst was comparable to commercial 40% PtRu/C. CO stripping test demonstrated the formation of highly active sites for CO oxidation on Pt/Mo_2C/C.

Porous trimetallic $Pt_{69}Rh_8Fe_{23}$ nanospheres supported on 2D $Ti_3C_2T_x$ MXene nanosheets as co-catalyst for EOR were also prepared via a one-step solvothermal route, where OAm was used as a mild reducing agent and solvent and CTAB as the capping agent and etchant [129]. The introduction of Rh and Fe not only facilitated the splitting of the C−C bond and the generation of oxygen-containing species, but also reduced the adsorption of CO−type intermediates. TEM studies (Fig. 6h) showed that ternary $Pt_{69}Rh_8Fe_{23}$ nanospheres of ca. 51.4 nm in diameter were dispersed homogeneously on the surface of MXene nanosheets, which delivered a peak current density of 3407.7 A g^{-1} and retention of 72.8% of the initial activity after 1000 successive cycles, as compared to 805.3 A g^{-1} and 58% of Pt/C TKK (Fig. 6i). The AOR performances of these different 2D metal oxides/hydroxides, metal carbides, and metal-based composites are also listed in Table 2.

6. Summary and perspectives

In this review, we summarized the preparation methods, unique

Table 2
Comparison of the alcohol oxidation performances with different 2D metal oxides/hydroxides, metal carbides, and metal-based composites.

Electrocatalyst	Electrolyte		Peak current from CV curves	Durability	Ref.
Ultrathin NiO nanosheets	Alkaline medium	1.0 M KOH and 0.5 M methanol	85.3 mA cm^{-2} vs. bulk NiO (23.9 mA cm^{-2}) at 50 mV s^{-1}	> 100% after 30,000 s at 0.5 V vs. Ag/AgCl	[92]
Porous NiCo$_2$O$_4$ nanosheets-assembled nanospheres		1.0 M KOH and 0.5 M methanol	40.9 mA mg^{-1} at 10 mV s^{-1}	~100% after 1000 s at 0.6 V vs. Hg/HgO	[95]
Ultrathin NiAl LDHs nanosheets		1.0 M NaOH and 1.0 M ethanol	543.33 mA mg^{-1}, 45.80 mA cm^{-2} vs. bulk NiAl LDHs (13.65 mA mg^{-1}, 1.17 mA cm^{-2}) at 50 mV s^{-1}	91.6% after 2000 s and 81.8% after 10,000 s at 0.58 V vs. Ag/AgCl	[90]
Hierarchical hollow Mn-doped Ni(OH)$_2$		1.0 M KOH and 0.5 M methanol	16.4 mA mg^{-1} vs. Ni(OH)$_2$ nanosheets (9.6 mA mg^{-1}) at 50 mV s^{-1}	> 90% after 1000 cycles	[101]
CuO/Co(OH)$_2$ nanosheets		1.0 M KOH and 3.0 M methanol	764 mA mg^{-1}, 159 mA cm^{-2} at 50 mV s^{-1}	~70% after 1000 cycles	[102]
Hierarchical NiCo$_2$O$_4$ nanoflowers-Ni(OH)$_2$ nanoparticles		1.0 M KOH and 0.5 M methanol	92.3 mA mg^{-1}, 132 mA cm^{-2} at 10 mV s^{-1}	~100% after 1000 s at 0.6 V vs. Ag/AgCl, 57.5% after 500 cycles	[103]
Pt nanoparticles-Fe$_2$O$_3$ nanosheets		1.0 M NaOH and 1.0 M methanol	181 mA mg^{-1} vs. Pt/C (563 mA mg^{-1}) at 50 mV s^{-1}	> 100% after 200 cycles	[122]
Pd nanoparticles-Ti$_3$C$_2$T$_x$ MXenes		1.0 M KOH and 1.0 M methanol	12.4 mA cm^{-2} vs. Pd/C (7.6 mA cm^{-2}) at 50 mV s^{-1}	~100% after 200 cycles	[126]
Pt$_{69}$Rh$_8$Fe$_{23}$ nanospheres- Ti$_3$C$_2$T$_x$ MXenes nanosheets		1.0 M KOH and 1.0 M ethanol	3407.7 mA mg^{-1}, 7.3 mA cm^{-2} vs. Pt/C (805.3 mA mg^{-1}, 3.3 mA cm^{-2}) at 50 mV s^{-1}	72.8% after 1000 cycles	[129]
Mesoporous WC nanoslices	Acidic medium	0.5 M H$_2$SO$_4$ and 1.0 M methanol	23.16 μA cm^{-2} vs. Pt/C (30.31 μA cm^{-2}) at 50 mV s^{-1}	N.A.	[115]
WC thin film		0.5 M H$_2$SO$_4$ and 2.0 M methanol	123.6 mA cm^{-2}	N.A.	[116]
Pt nanoparticles-ultrathin WO$_3$ nanosheets		0.5 M H$_2$SO$_4$ and 1.0 M methanol	1250 mA mg^{-1}, 2.27 mA cm^{-2} vs. Pt/C (320 mA mg^{-1}, 0.77 mA cm^{-2}) at 50 mV s^{-1}	~80% after 1000 cycles	[121]
Pt nanoparticles-Ti$_3$C$_2$ nanosheets		0.5 M H$_2$SO$_4$ and 0.5 M methanol	1.137 mA cm^{-2} vs. Pt/C (0.388 mA cm^{-2}) at 50 mV s^{-1}	0.04 mA cm^{-2} retained after 7200 s at 0.6 V vs. Hg/Hg$_2$SO$_4$	[127]
Pt nanoparticles-Mo$_2$C		0.05 M H$_2$SO$_4$ and 1.0 M ethanol	650 mA mg^{-1} vs. Pt/C (50 mA mg^{-1}) at 50 mV s^{-1}	~35% after 3500 s at 0.6 V vs. RHE	[128]

structures, and corresponding AOR performances (specific activity and durability) of a range of 2D functional nanostructures, including noble metals and alloys, transition metal oxides/hydroxides, transition metal carbides, and precious metal-based composites. Effective electrocatalysts are identified to possess a high activity towards the dehydrogenation of alcohols, production of oxygen-containing species, adsorption of CO and OH species, and effective $C-C$ bond cleavage.

There are at least four critical factors in the design and engineering of these 2D electrocatalysts: (i) elemental composition that dictates the intrinsic electrocatalytic activity; (ii) size and surface morphology that impact the mass transfer and accessibility of catalytic active sites; (iii) interfacial interaction for the reduction of energetic barrier for charge transport and suppression of unwanted side reactions; and (iv) synergistic interactions between structural components in nanocomposites to manipulate adsorption of important reaction intermediates and hence electrocatalytic activity.

Despite substantial progress in recent years, critical issues remain. Notably, noble metal nanostructures have remained the leading catalysts towards AOR. Further structural engineering is needed to reduce their use (cost) without compromising the electrocatalytic performance. Concurrently, development of noble metal-free, viable alternatives is urgently needed. Towards this end, a major obstacle is the lack of in-depth understanding of the catalytic mechanisms (in particular, unambiguous identification of the catalytic active sites). This presents particular challenges in the utilization of C_{2+} alcohols (i.e., ethanol, propanol, ethylene glycol, glycerol, etc.) as fuels, due to the high energy barrier in breaking the $C-C$ bonds and hence the difficulty in improving the fuel cell performance to a new level. Towards this end, a deliberate integration of state-of-the-art theoretical simulations and modeling into rational material design represents a unique route. In addition, development of effective strategies for the preparation of such 2D catalysts is critically needed, in particular, with select surface morphologies, structural defects, and crystalline phases. Furthermore, in situ and operando analysis of the catalyst structure is strongly desired to unravel the mechanistic contributions to the electrocatalytic activity, in particular, for multicomponent nanocomposite catalysts.

Declaration of Competing Interest

The authors declare that they have no known competing financial interests or personal relationships that could have appeared to influence the work reported in this paper.

Acknowledgments

References

[1] M. Dresselhaus, I. Thomas, Alternative energy technologies, Nature 414 (2001) 332–337.
[2] S. Chu, A. Majumdar, Opportunities and challenges for a sustainable energy future, Nature 488 (2012) 294–303.
[3] B. Dunn, H. Kamath, J. Tarascon, Electrical Energy Storage for the Grid: A Battery of Choices, Science 334 (2011) 928–935.
[4] M. Winter, R. Brodd, What are batteries, fuel cells, and supercapacitors? Chem. Rev. 104 (2004) 4245–4269.
[5] B. Steele, A. Heinzel, Materials for fuel-cell technologies, Nature 414 (2001) 345–352.
[6] M. Armand, J. Tarascon, Building better batteries, Nature 451 (2008) 652–657.
[7] B. Logan, B. Hamelers, R. Rozendal, U. Schrorder, J. Keller, S. Freguia, P. Aelterman, W. Verstraete, K. Rabaey, Microbial fuel cells: Methodology and technology, Environ. Sci. Technol. 40 (2006) 5181–5192.
[8] M. Debe, Electrocatalyst approaches and challenges for automotive fuel cells, Nature 486 (2012) 43–51.
[9] A. Brouzgou, S. Song, P. Tsiakaras, Low and non-platinum electrocatalysts for PEMFCs: Current status, challenges and prospects, Appl. Catal. B-Environ. 127 (2012) 371–388.
[10] A. Brouzgou, A. Podias, P. Tsiakaras, PEMFCs and AEMFCs directly fed with ethanol: a current status comparative review, J. Appl. Electrochem. 43 (2013) 119–136.
[11] C. Bianchini, P. Shen, Palladium-Based Electrocatalysts for Alcohol Oxidation in Half Cells and in Direct Alcohol Fuel Cells, Chem. Rev. 109 (2009) 4183–4206.
[12] J. Liu, Q. Ma, Z. Huang, G. Liu, H. Zhang, Recent Progress in Graphene-Based Noble-Metal Nanocomposites for Electrocatalytic Applications, Adv. Mater. 31 (2019) 1800696.
[13] C. Lamy, A. Lima, V. LeRhun, F. Delime, C. Coutanceau, J. Leger, Recent advances in the development of direct alcohol fuel cells (DAFC), J. Power Sources 105 (2002) 283–296.
[14] Q. Lu, Y. Yu, Q. Ma, B. Chen, H. Zhang, 2D Transition-Metal-Dichalcogenide-Nanosheet-Based Composites for Photocatalytic and Electrocatalytic Hydrogen Evolution Reactions, Adv. Mater. 28 (2016) 1917–1933.
[15] Y. Zhong, X. Xia, F. Shi, J. Zhan, J. Tu, H. Fan, Transition Metal Carbides and Nitrides in Energy Storage and Conversion, Adv. Sci. 3 (2016) 1500286.
[16] Y. Wang, Y. Zhang, Z. Liu, C. Xie, S. Feng, D. Liu, M. Shao, S. Wang, Layered Double Hydroxide Nanosheets with Multiple Vacancies Obtained by Dry Exfoliation as Highly Efficient Oxygen Evolution Electrocatalysts, Angew. Chem.-Int. Edit. 56 (2017) 5867–5871.
[17] Y. Xu, M. Kraft, R. Xu, Metal-free carbonaceous electrocatalysts and photocatalysts for water splitting, Chem. Soc. Rev. 45 (2016) 3039–3052.
[18] J. Bai, D. Liu, J. Yang, Y. Chen, Nanocatalysts for Electrocatalytic Oxidation of Ethanol, ChemSusChem 12 (2019) 2117–2132.
[19] A. Ehsani, A. Heidari, R. Asgari, Electrocatalytic Oxidation of Ethanol on the Surface of Graphene Based Nanocomposites: An Introduction and Review to it in Recent Studies, Chem. Rec. 19 (2019) 2341–2360.
[20] E. Antolini, Catalysts for direct ethanol fuel cells, J. Power Sources 170 (2007) 1–12.
[21] Y. Tong, X. Yan, J. Liang, S. Dou, Metal-based electrocatalysts for methanol electro-oxidation: Progress, opportunities, and challenges, Small 1904126 (n.d.).
[22] M. Mansor, S. Timmiati, K. Lim, W. Wong, S. Kamarudin, N. Kamarudin, Recent progress of anode catalysts and their support materials for methanol electro-oxidation reaction, Int. J. Hydrogen Energy 44 (2019) 14744–14769.
[23] A. Ali, P. Shen, Recent advances in graphene-based platinum and palladium electrocatalysts for the methanol oxidation reaction, J. Mater. Chem. A 7 (2019) 22189–22217.
[24] M. Kamarudin, S. Kamarudin, M. Masdar, W. Daud, Review: Direct ethanol fuel cells, Int. J. Hydrogen Energy 38 (2013) 9438–9453.
[25] S. Siwal, S. Thakur, Q. Zhang, V. Thakur, Electrocatalysts for electrooxidation of direct alcohol fuel cell: chemistry and applications, Mater. Today Chem. 14 (2019) 100182.
[26] Y. Jiao, Y. Zheng, M. Jaroniec, S. Qiao, Design of electrocatalysts for oxygen- and hydrogen-involving energy conversion reactions, Chem. Soc. Rev. 44 (2015) 2060–2086.
[27] R. Bashyam, P. Zelenay, A class of non-precious metal composite catalysts for fuel cells, Nature 443 (2006) 63–66.
[28] S. Shen, T. Zhao, J. Xu, Y. Li, Synthesis of PdNi catalysts for the oxidation of ethanol in alkaline direct ethanol fuel cells, J. Power Sources 195 (2010) 1001–1006.
[29] C. Alegre, M. Gálvez, R. Moliner, V. Baglio, A. Stassi, A. Aricò, M. Lázaro, Platinum Ruthenium Catalysts Supported on Carbon Xerogel for Methanol Electro-Oxidation: Influence of the Catalyst Synthesis Method, ChemCatChem 5 (2013) 3770–3780.
[30] J. Zhang, S. Lu, Y. Xiang, S.P. Jiang, Intrinsic effect of carbon supports on the activity and stability of precious metal based catalysts for electrocatalytic alcohol oxidation in fuel cells: A review, ChemSusChem 13 (2020) 2484–2502.
[31] K. Cheung, W. Wong, D. Ma, T. Lai, K. Wong, Transition metal complexes as electrocatalysts—Development and applications in electro-oxidation reactions, Coordin. Chem. Rev. 251 (2007) 2367–2385.
[32] G. Chen, H. Wan, W. Ma, N. Zhang, Y. Cao, X. Liu, J. Wang, R. Ma, Layered Metal Hydroxides and Their Derivatives: Controllable Synthesis, Chemical Exfoliation, and Electrocatalytic Applications, Adv. Energy Mater. 10 (2020) 1902535.
[33] D. Ham, J. Lee, Transition Metal Carbides and Nitrides as Electrode Materials for Low Temperature Fuel Cells, Energies 2 (2009) 873–899.
[34] Y. Li, S. Guo, Noble metal-based 1D and 2D electrocatalytic nanomaterials: Recent progress, challenges and perspectives, Nano Today 28 (2019) 100774.
[35] Z. Yin, L. Lin, D. Ma, Construction of Pd-based nanocatalysts for fuel cells: opportunities and challenges, Catal. Sci. Technol. 4 (2014) 4116–4128.
[36] K. Ozoemena, Nanostructured platinum-free electrocatalysts in alkaline direct alcohol fuel cells: catalyst design, principles and applications, RSC Adv. 6 (2016) 89523–89550.
[37] Y. Lu, S. Du, R. Steinberger-Wilckens, One-dimensional nanostructured electrocatalysts for polymer electrolyte membrane fuel cells—A review, Appl. Catal. B-Environ. 199 (2016) 292–314.
[38] X. Li, J. Wang, One-dimensional and two-dimensional synergized nanostructures for high-performing energy storage and conversion, InfoMat 2 (2020) 3–32.
[39] C. Koenigsmann, W. Zhou, R. Adzic, E. Sutter, S. Wong, Size-Dependent Enhancement of Electrocatalytic Performance in Relatively Defect-Free, Processed Ultrathin Platinum Nanowires, Nano Lett. 10 (2010) 2806–2811.

[40] T. Meng, M. Cao, Transition Metal Carbide Complex Architectures for Energy-Related Applications, Chem. Eur. J. 24 (2018) 16716–16736.

[41] S. Mao, G. Lu, J. Chen, Three-dimensional graphene-based composites for energy applications, Nanoscale 7 (2015) 6924–6943.

[42] M. Nazarian-Samani, H. Kim, S. Park, H. Youn, D. Mhamane, S. Lee, M. Kim, J. Jeong, S. Haghighat-Shishavan, K. Roh, S. Kashani-Bozorg, K. Kim, Three-dimensional graphene-based spheres and crumpled balls: micro- and nano-structures, synthesis strategies, properties and applications, RSC Adv. 6 (2016) 50941–50967.

[43] Z. Liang, H. Zheng, R. Cao, Importance of Electrocatalyst Morphology for the Oxygen Reduction Reaction, ChemElectroChem 6 (2019) 2600–2614.

[44] X. Zhao, L. Mao, Q. Cheng, J. Li, F. Liao, G. Yang, L. Xie, C. Zhao, L. Chen, Two-dimensional Spinel Structured Co-based Materials for High Performance Supercapacitors: A Critical Review, Chem. Eng. J. 387 (2020) 124081.

[45] X. Chia, M. Pumera, Characteristics and performance of two-dimensional materials for electrocatalysis, Nat. Catal. 1 (2018) 909–921.

[46] N. Bagkar C., H. Chen M., H. Parab, R. Liu, Nanostructured Electrocatalyst Synthesis: Fundamental and Methods, in: H. Liu, J. Zhang (Eds.), Electrocatalysis of Direct Methanol Fuel Cells: From Fundamentals to Applications, Wiley, Weinheim, 2009, pp. 79–114.

[47] Q. Sun, H. Xu, Y. Du, Recent Achievements in Noble Metal Catalysts with Unique Nanostructures for Liquid Fuel Cells, ChemSusChem 13 (2020) 2540–2551.

[48] A.S. Aricò, V. Baglio, V. Antonucci, Direct methanol fuel cells: History, status and perspectives, in: H. Liu, J. Zhang (Eds.), Electrocatalysis of Direct Methanol Fuel Cells, Wiley, Weinheim, 2009, pp. 1–78.

[49] A. Hamnett, Mechanism and electrocatalysis in the direct methanol fuel cell, Catal. Today 38 (1997) 445–457.

[50] X. Li, A. Faghri, Review and advances of direct methanol fuel cells (DMFCs) part I: Design, fabrication, and testing with high concentration methanol solutions, J. Power Sources 226 (2013) 223–240.

[51] H. Liu, C. Song, L. Zhang, J. Zhang, H. Wang, D. Wilkinson, A review of anode catalysis in the direct methanol fuel cell, J. Power Sources 155 (2006) 95–110.

[52] E. Yu, U. Krewer, K. Scott, Principles and Materials Aspects of Direct Alkaline Alcohol Fuel Cells, Energies 3 (2010) 1499–1528.

[53] J. Maya-Cornejo, R. Carrera-Cerritos, D. Sebastián, J. Ledesma-García, L. Arriaga, A. Aricò, V. Baglio, PtCu catalyst for the electro-oxidation of ethanol in an alkaline direct alcohol fuel cell, Int. J. Hydrogen Energy 42 (2017) 27919–27928.

[54] H. Xu, P. Song, Y. Zhang, Y. Du, 3D–2D heterostructure of PdRu/NiZn oxyphosphides with improved durability for electrocatalytic methanol and ethanol oxidation, Nanoscale 10 (2018) 12605–12611.

[55] J. Chen, S. Lim, C. Kuo, H. Tuan, Sub-1 nm PtSn ultrathin sheet as an extraordinary electrocatalyst for methanol and ethanol oxidation reactions, J. Colloid Interface Sci. 545 (2019) 54–62.

[56] P. Joghee, J. Malik, S. Pylypenko, R. O'Hayre, A review on direct methanol fuel cells – In the perspective of energy and sustainability, MRS Energy Sustain. 2 (2015) E3.

[57] J. Tiwari, R. Tiwari, G. Singh, K. Kim, Recent progress in the development of anode and cathode catalysts for direct methanol fuel cells, Nano Energy 2 (2013) 553–578.

[58] J. Calderón Gómez, R. Moliner, M. Lázaro, Palladium-Based Catalysts as Electrodes for Direct Methanol Fuel Cells, A Last Ten Years Review, Catalysts 6 (2016) 130.

[59] Y. Wang, S. Zou, W. Cai, Recent Advances on Electro-Oxidation of Ethanol on Pt- and Pd-Based Catalysts: From Reaction Mechanisms to Catalytic Materials, Catalysts 5 (2015) 1507–1534.

[60] Z. Liang, T. Zhao, J. Xu, L. Zhu, Mechanism study of the ethanol oxidation reaction on palladium in alkaline media, Electrochim. Acta 54 (2009) 2203–2208.

[61] A. Serov, C. Kwak, Recent achievements in direct ethylene glycol fuel cells (DEGFC), Appl. Catal. B-Environ. 97 (2010) 1–12.

[62] L. An, R. Chen, Recent progress in alkaline direct ethylene glycol fuel cells for sustainable energy production, J. Power Sources 329 (2016) 484–501.

[63] E. Antolini, Glycerol Electro-Oxidation in Alkaline Media and Alkaline Direct Glycerol Fuel Cells, Catalysts 9 (2019) 980.

[64] M. Davi, D. Kessler, A. Slabon, Electrochemical oxidation of methanol and ethanol on two-dimensional self-assembled palladium nanocrystal arrays, Thin Solid Films 615 (2016) 221–225.

[65] M. Farsadrooh, J. Torrero, L. Pascual, M. Pena, M. Retuerto, S. Rojas, Two-dimensional Pd-nanosheets as efficient electrocatalysts for ethanol electrooxidation. Evidences of the C-C scission at low potentials, Appl. Catal. B-Environ. 237 (2018) 866–875.

[66] M. Davi, T. Schultze, D. Kleinschmidt, F. Schiefer, B. Hahn, A. Slabon, Gold nanocrystal arrays as electrocatalysts for the oxidation of methanol and ethanol, Z. Naturforsch. B 71 (2016) 821–825.

[67] H. Liu, J. Qin, S. Zhao, Z. Gao, Q. Fu, Y. Song, Two-dimensional circular platinum nanodendrites toward efficient oxygen reduction reaction and methanol oxidation reaction, Electrochem. Commun. 98 (2019) 53–57.

[68] J. Zhu, S. Chen, Q. Xue, F. Li, H. Yao, L. Xu, Y. Chen, Hierarchical porous Rh nanosheets for methanol oxidation reaction, Appl. Catal. B-Environ. 264 (2020) 118520.

[69] Y. Kang, Q. Xue, P. Jin, J. Jiang, J. Zeng, Y. Chen, Rhodium Nanosheets-Reduced Graphene Oxide Hybrids: A Highly Active Platinum-Alternative Electrocatalyst for the Methanol Oxidation Reaction in Alkaline Media, ACS Sustain. Chem. Eng. 5 (2017) 10156–10162.

[70] S. Xing, Z. Liu, Q. Xue, S. Yin, F. Li, W. Cai, S. Li, P. Chen, P. Jin, H. Yao, Y. Chen, Rh nanoroses for isopropanol oxidation reaction, Appl. Catal. B-Environ. 259 (2019) 118082.

[71] S. Han, H. Liu, P. Chen, J. Jiang, Y. Chen, Porous Trimetallic PtRhCu Cubic Nanoboxes for Ethanol Electrooxidation, Adv. Energy Mater. 8 (2018) 1801326.

[72] Y. Kang, Q. Xue, Y. Zhao, X. Li, P. Jin, Y. Chen, Selective Etching Induced Synthesis of Hollow Rh Nanospheres Electrocatalyst for Alcohol Oxidation Reactions, Small 14 (2018) 1801239.

[73] Y. Kang, F. Li, S. Li, P. Ji, J. Zeng, J. Jiang, Y. Chen, Unexpected catalytic activity of rhodium nanodendrites with nanosheet subunits for methanol electrooxidation in an alkaline medium, Nano Res. 9 (2016) 3893–3902.

[74] J. Ge, P. Wei, G. Wu, Y. Liu, T. Yuan, Z. Li, Y. Qu, Y. Wu, H. Li, Z. Zhuang, X. Hong, Y. Li, Ultrathin Palladium Nanomesh for Electrocatalysis, Angew. Chem.-Int. Edit. 57 (2018) 3435–3438.

[75] N.S. Marinkovic, M. Li, R.R. Adzic, Pt-based catalysts for electrochemical oxidation of ethanol, Top. Curr. Chem. 377 (2019) 11.

[76] S. Peera, T. Lee, A. Sahu, Pt-rare earth metal alloy/metal oxide catalysts for oxygen reduction and alcohol oxidation reactions: an overview, Sustain. Energy Fuels 3 (2019) 1866–1891.

[77] F. Gao, Y. Zhang, F. Ren, Y. Shiraishi, Y. Du, Universal Surfactant-Free Strategy for Self-Standing 3D Tremella-Like Pd–M (M = Ag, Pb, and Au) Nanosheets for Superior Alcohols Electrocatalysis, Adv. Funct. Mater. 30 (2020) 2000255.

[78] Y. Qin, M. Luo, Y. Sun, C. Li, B. Huang, Y. Yang, Y. Li, L. Wang, S. Guo, Intermetallic *hcp*-PtBi/*fcc*-Pt Core/Shell Nanoplates Enable Efficient Bifunctional Oxygen Reduction and Methanol Oxidation Electrocatalysis, ACS Catal. 8 (2018) 5581–5590.

[79] X. Guo, H. Shang, J. Guo, H. Xu, Y. Du, Ultrafine two-dimensional alloyed PdCu nanosheets-constructed three-dimensional nanoflowers enable efficient ethylene glycol electrooxidation, Appl. Surf. Sci. 481 (2019) 1532–1537.

[80] L. Jin, H. Xu, C. Chen, H. Shang, Y. Wang, C. Wang, Y. Du, Three-dimensional PdCuM (M = Ru, Rh, Ir) Trimetallic Alloy Nanosheets for Enhancing Methanol Oxidation Electrocatalysis, ACS Appl. Mater. Interfaces 11 (2019) 42123–42130.

[81] M. Shen, Y. Huang, D. Wu, J. Lu, M. Cao, M. Liu, Y. Yang, H. Li, B. Guo, R. Cao, Facile ultrafine copper seed-mediated approach for fabricating quasi-two-dimensional palladium-copper bimetallic trigonal hierarchical nanoframes, Nano Res. 10 (2017) 2810–2822.

[82] H. Lv, L. Sun, D. Xu, S. Suib, B. Liu, One-pot aqueous synthesis of ultrathin trimetallic PdPtCu nanosheets for the electrooxidation of alcohols, Green Chem. 21 (2019) 2367–2374.

[83] C. Shang, Y. Guo, E. Wang, Integration of two-dimensional morphology and porous surfaces to boost methanol electrooxidation performances of PtAg alloy nanomaterials, Nano Res. 11 (2018) 6375–6383.

[84] Z. Yin, Y. Zheng, H. Wang, J. Li, Q. Zhu, Y. Wang, N. Ma, G. Hu, B. He, A. Knop-Gericke, R. Schlog, D. Ma, Engineering Interface with One-Dimensional Co₃O₄ Nanostructure in Catalytic Membrane Electrode: Toward an Advanced Electrocatalyst for Alcohol Oxidation, ACS Nano 11 (2017) 12365–12377.

[85] S. Candelaria, N. Bedford, T. Woehl, N. Rentz, A. Showalter, S. Pylypenko, B. Bunker, S. Lee, B. Reinhart, Y. Ren, S. Ertem, E. Coughlin, N. Sather, J. Horan, A. Herring, L. Greenleette, Multi-Component Fe-Ni Hydroxide Nanocatalyst for Oxygen Evolution and Methanol Oxidation Reactions under Alkaline Conditions, ACS Catal. 7 (2017) 365–379.

[86] P. Manivasakan, P. Ramasamy, J. Kim, Use of urchin-like Ni$_x$Co$_{3-x}$O$_4$ hierarchical nanostructures based on non-precious metals as bifunctional electrocatalysts for anion-exchange membrane alkaline alcohol fuel cells, Nanoscale 6 (2014) 9665–9672.

[87] X. Zou, A. Goswami, T. Asefa, Efficient Noble Metal-Free (Electro)Catalysis of Water and Alcohol Oxidations by Zinc-Cobalt Layered Double Hydroxide, J. Am. Chem. Soc. 135 (2013) 17242–17245.

[88] A. Golikand, M. Asgari, M. Maragheh, S. Shahrokhian, Methanol electrooxidation on a nickel electrode modified by nickel-dimethylglyoxime complex formed by electrochemical synthesis, J. Electroanal. Chem. 588 (2006) 155–160.

[89] A. Golikand, S. Shahrokhian, M. Asgari, M. Maragheh, I. Irannejad, A. Khanchi, Electrocatalytic oxidation of methanol on a nickel electrode modified by nickel dimethylglyoxime complex in alkaline medium, J. Power Sources 144 (2005) 21–27.

[90] L. Xu, Z. Wang, X. Chen, Z. Qu, F. Li, W. Yang, Ultrathin layered double hydroxide nanosheets with Ni(III) active species obtained by exfoliation for highly efficient ethanol electrooxidation, Electrochim. Acta 260 (2018) 898–904.

[91] T. Zhang, M. Wu, D. Yan, J. Mao, H. Liu, W. Hu, X. Du, T. Ling, S. Qiao, Engineering oxygen vacancy on NiO nanorod arrays for alkaline hydrogen evolution, Nano Energy 43 (2018) 103–109.

[92] W. Yang, X. Yang, J. Jia, C. Hou, H. Gao, Y. Mao, C. Wang, J. Lin, X. Luo, Oxygen vacancies confined in ultrathin nickel oxide nanosheets for enhanced electrocatalytic methanol oxidation, Appl. Catal. B-Environ. 244 (2019) 1096–1102.

[93] X. Guo, C. Chen, Y. Zhang, Y. Xu, H. Pang, The application of transition metal cobaltites in electrochemistry, Energy Storage Mater. 23 (2019) 439–465.

[94] X. Gao, H. Zhang, Q. Li, X. Yu, Z. Hong, X. Zhang, C. Liang, Z. Lin, Hierarchical NiCo₂O₄ Hollow Microcuboids as Bifunctional Electrocatalysts for Overall Water-Splitting, Angew. Chem.-Int. Edit. 55 (2016) 6290–6294.

[95] L. Gu, L. Qian, Y. Lei, Y. Wang, J. Li, H. Yuan, D. Xiao, Microwave-assisted synthesis of nanosphere-like NiCo₂O₄ consisting of porous nanosheets and its application in electro-catalytic oxidation of methanol, J. Power Sources 261 (2014) 317–323.

[96] H. Yin, Z. Tang, Ultrathin two-dimensional layered metal hydroxides: an emerging platform for advanced catalysis, energy conversion and storage, Chem. Soc. Rev. 45 (2016) 4873–4891.

[97] X. Li, D. Du, Y. Zhang, W. Xing, Q. Xue, Z. Yan, Layered double hydroxides toward high-performance supercapacitors, J. Mater. Chem. A 5 (2017) 15460–15485.

[98] X. Long, Z. Wang, S. Xiao, Y. An, S. Yang, Transition metal based layered double

hydroxides tailored for energy conversion and storage, Mater. Today 19 (2016) 213–226.

[99] M. Shao, R. Zhang, Z. Li, M. Wei, D. Evans, X. Duan, Layered double hydroxides toward electrochemical energy storage and conversion: design, synthesis and applications, Chem. Commun. 51 (2015) 15880–15893.

[100] X. Gao, P. Wang, Z. Pan, J. Claverie, J. Wang, Recent Progress in Two-Dimensional Layered Double Hydroxides and Their Derivatives for Supercapacitors, ChemSusChem 13 (2020) 1226–1254.

[101] B. Dong, W. Li, X. Huang, Z. Ali, T. Zhang, Z. Yang, Y. Hou, Fabrication of hierarchical hollow Mn doped Ni(OH)$_2$ nanostructures with enhanced catalytic activity towards electrochemical oxidation of methanol, Nano Energy 55 (2019) 37–41.

[102] L. Chen, Z. Hua, J. Shi, M. He, CuO/Co(OH)$_2$ Nanosheets: A Novel Kind of Electrocatalyst for Highly Efficient Electrochemical Oxidation of Methanol, ACS Appl. Mater. Interfaces 10 (2018) 39002–39008.

[103] B. Wang, Y. Cao, Y. Chen, R. Wang, X. Wang, X. Lai, C. Xiao, J. Tu, S. Ding, Microwave-assisted fast synthesis of hierarchical Ni(OH)$_2$ nanoflower-like supported Ni(OH)$_2$ nanoparticles with an enhanced electrocatalytic activity towards methanol oxidation, Inorg. Chem. Front. 5 (2018) 172–182.

[104] R. Ganesan, J. Lee, Tungsten carbide microspheres as a noble-metal-economic electrocatalyst for methanol oxidation, Angew. Chem.-Int. Edit. 44 (2005) 6557–6560.

[105] Y. Wang, C. He, A. Brouzgou, Y. Liang, R. Fu, D. Wu, P. Tsiakaras, S. Song, A facile soft-template synthesis of ordered mesoporous carbon/tungsten carbide composites with high surface area for methanol electrooxidation, J. Power Sources 200 (2012) 8–13.

[106] X. Yang, Y. Kimmel, J. Fu, B. Koel, J. Chen, Activation of Tungsten Carbide Catalysts by Use of an Oxygen Plasma Pretreatment, ACS Catal. 2 (2012) 765–769.

[107] C. Di Valentin, D. Fittipaldi, G. Pacchioni, Methanol Oxidation Reaction on α-Tungsten Carbide Versus Platinum (111) Surfaces: A DFT Electrochemical Study, ChemCatChem 7 (2015) 3533–3543.

[108] W. Zheng, L. Chen, C. Ma, Density functional study of H$_2$O adsorption and dissociation on WC(0001), Comput. Theor. Chem. 1039 (2014) 75–80.

[109] A. Stottlemyer, E. Weigert, J. Chen, Tungsten Carbides as Alternative Electrocatalysts: From Surface Science Studies to Fuel Cell Evaluation, Ind. Eng. Chem. Res. 50 (2011) 16–22.

[110] G. Song, M. Shi, Y. Chu, C. Ma, Synthesis and characterization of highly dispersed Pt-TiO$_2$ vertical bar WC/BC as anode catalyst for methanol oxidation, Electrochim. Acta 112 (2013) 53–58.

[111] M. Shi, P. Yang, L. Huang, H. Chen, X. Mao, Heterostructures in carbon-doped tungsten nitride and its effect on electrocatalytic properties for methanol oxidation, Electrochim. Acta 238 (2017) 210–219.

[112] Y. Zhou, X. Li, C. Yu, X. Hu, Y. Yin, S. Guo, S. Zhong, Synergistic and Durable Pt-WC Catalyst for Methanol Electro-Oxidation in Ionic Liquid Aqueous Solution, ACS Appl. Energy Mater. 2 (2019) 8459–8463.

[113] M. Roca-Ayats, G. Garcia, M. Pena, M. Martinez-Huerta, Titanium carbide and carbonitride electrocatalyst supports: modifying Pt-Ti interface properties by

[114] M. Obradovic, B. Babic, V. Radmilovic, N. Krstajic, S. Gojkovic, Core-shell structured tungsten-tungsten carbide as a Pt catalyst support and its activity for methanol electrooxidation, Int. J. Hydrogen Energy 37 (2012) 10671–10679.

[115] J. Gao, S. Wu, J. Chen, Y. Li, G. Li, Mesoporous tungsten carbide nanoslices with pure phase and superior electrocatalysis, Electrochim. Acta 222 (2016) 728–734.

[116] H. Zheng, C. Ma, J. Huang, G. Li, Plasma enhanced chemical vapor deposition nanocrystalline tungsten carbide thin film and its electro-catalytic activity, J. Mater. Sci. Technol. 21 (2005) 545–548.

[117] W. Wang, Y. Yang, Y. Liu, Z. Zhang, W. Dong, Z. Lei, Hybrid NiCoO$_x$ adjacent to Pd nanoparticles as a synergistic electrocatalyst for ethanol oxidation, J. Power Sources 273 (2015) 631–637.

[118] E. Umeshbabu, G. Rao, A Vanadium(V) Oxide Nanorod Promoted Platinum/Reduced Graphene Oxide Electrocatalyst for Alcohol Oxidation under Acidic Conditions, ChemPhysChem 17 (2016) 3524–3534.

[119] S. Das, K. Dutta, Y. Shul, P. Kundu, Progress in Developments of Inorganic Nanocatalysts for Application in Direct Methanol Fuel Cells, Crit. Rev. Solid State 40 (2015) 316–357.

[120] J. Zeng, C. Francia, C. Gerbaldi, V. Baglio, S. Specchia, A. Aricò, P. Spinelli, Hybrid ordered mesoporous carbons doped with tungsten trioxide as supports for Pt electrocatalysts for methanol oxidation reaction, Electrochim. Acta 94 (2013) 80–91.

[121] Y. Zhang, Y. Shi, R. Chen, L. Tao, C. Xie, D. Liu, D. Yan, S. Wang, Enriched nucleation sites for Pt deposition on ultrathin WO$_3$ nanosheets with unique interactions for methanol oxidation, J. Mater. Chem. A 6 (2018) 23028–23033.

[122] Z. Zhang, M. Ye, E. Harvey, G. Merle, Methanol Electrooxidation with Platinum Decorated Hematene Nanosheet, J. Electrochem. Soc. 166 (2019) H135–H139.

[123] G. Cui, P. Shen, H. Meng, J. Zhao, G. Wu, Tungsten carbide as supports for Pt electrocatalysts with improved CO tolerance in methanol oxidation, J. Power Sources 196 (2011) 6125–6130.

[124] Y. Ou, X. Cui, X. Zhang, Z. Jiang, Titanium carbide nanoparticles supported Pt catalysts for methanol electrooxidation in acidic media, J. Power Sources 195 (2010) 1365–1369.

[125] J. Yang, Y. Xie, R. Wang, B. Jiang, C. Tian, G. Mu, J. Yin, B. Wang, H. Fu, Synergistic Effect of Tungsten Carbide and Palladium on Graphene for Promoted Ethanol Electrooxidation, ACS Appl. Mater. Interfaces 5 (2013) 6571–6579.

[126] Z. Liang, Z. Zhuang, S. Li, L. Xia, Y. Zhao, Y. Zhao, C. Han, L. Zhou, MXene Surface Terminations Enable Strong Metal-Support Interactions for Efficient Methanol Oxidation on Palladium, ACS Appl. Mater. Interfaces 12 (2020) 2400–2406.

[127] Y. Wang, J. Wang, G. Han, C. Du, Q. Deng, Y. Gao, G. Yin, Y. Song, Pt decorated Ti$_3$C$_2$ MXene for enhanced methanol oxidation reaction, Ceram. Int. 45 (2019) 2411–2417.

[128] L. Lin, W. Sheng, S. Yao, D. Ma, J. Chen, Pt/Mo$_2$C/C-cp as a highly active and stable catalyst for ethanol electrooxidation, J. Power Sources 345 (2017) 182–189.

[129] P. Wang, H. Cui, C. Wang, In situ formation of porous trimetallic PtRhFe nanospheres decorated on ultrathin MXene nanosheets as highly efficient catalysts for ethanol oxidation, Nano Energy 66 (2019) 104196.